

1                   **Evolutionary shaping of human brain dynamics**

2     James C. Pang<sup>1,2\*</sup>, James K. Rilling<sup>3,4,5</sup>, James A. Roberts<sup>2†</sup>, Martijn P. van den Heuvel<sup>6,7†</sup>, Luca  
3     Cocchi<sup>2\*†</sup>

4     <sup>1</sup>The Turner Institute for Brain and Mental Health, School of Psychological Sciences, and Monash  
5     Biomedical Imaging, Monash University, Victoria, Australia

6     <sup>2</sup>QIMR Berghofer Medical Research Institute, Queensland, Australia

7     <sup>3</sup>Department of Anthropology, Emory University, Atlanta, Georgia, USA

8     <sup>4</sup>Department of Psychiatry and Behavioral Sciences, Emory University, Atlanta, Georgia, USA

9     <sup>5</sup>Yerkes National Primate Research Center, Emory University, Atlanta, Georgia, USA

10    <sup>6</sup>Department of Complex Traits Genetics, Center for Neurogenetics and Cognitive Research, Vrije  
11    Universiteit Amsterdam, Amsterdam, Netherlands

12    <sup>7</sup>Department of Clinical Genetics, Amsterdam UMC, Vrije Universiteit Amsterdam, Amsterdam,  
13    Netherlands

14    \*Correspondence: [james.pang1@monash.edu](mailto:james.pang1@monash.edu) (J.C.P.), [luca.cocchi@qimrberghofer.edu.au](mailto:luca.cocchi@qimrberghofer.edu.au) (L.C.)

15    †These authors contributed equally to this work

19                   **ABSTRACT**

20    The human brain is distinct from those of other species in terms of size, organization, and  
21    connectivity. How do structural evolutionary differences drive patterns of neural activity enabling  
22    brain function? Here, we combine brain imaging and biophysical modeling to show that the  
23    anatomical wiring of the human brain distinctly shapes neural dynamics. This shaping is  
24    characterized by a narrower distribution of dynamic ranges across brain regions compared with  
25    that of chimpanzees, our closest living primate relatives. We find that such a narrow dynamic range  
26    distribution supports faster integration between regions, particularly in transmodal systems.  
27    Conversely, a broad dynamic range distribution as seen in chimpanzees facilitates brain processes  
28    relying more on neural interactions within specialized local brain systems. These findings suggest  
29    that human brain dynamics have evolved to foster rapid associative processes in service of  
30    complex cognitive functions and behavior.

31 **INTRODUCTION**

32 An important and unresolved problem in neuroscience is how connectivity, from neurons to  
33 macroscopic brain regions, can give rise to the complex dynamics that underlie behavior and  
34 advanced cognitive functions [1]. Identifying special features of the human brain that have evolved  
35 to support these complex neural dynamics is key in tackling this open question.

36 It is known that the human brain is approximately three times larger than would be expected in a  
37 primate with the same body mass [2,3]. Beyond general growth, neuroimaging analyses via  
38 magnetic resonance imaging (MRI) have indicated that a greater proportion of the human brain's  
39 cortical surface is allocated to higher-order association cortices compared to primary sensory and  
40 motor areas [4–6]. This expansion of association areas is accompanied by increased anatomical  
41 connectivity [7], providing a structural substrate assumed to enable efficient region-to-region  
42 communication and integration of remote neural processes. Studies of the brain's structural wiring,  
43 known as the *human connectome*, have shown widespread overlapping topological properties (e.g.,  
44 small-world and modularity properties [7]) with those of other primates (like macaque and  
45 chimpanzees), accompanied by subtle but potentially consequential species differences [8].

46 Here, we ask how do the abovementioned structural changes shape whole-brain patterns of neural  
47 activity supporting brain function. To address this knowledge gap, we combine MRI data with  
48 advanced biophysical modeling to generate neural dynamics supported by the human connectome  
49 and the connectome of one of our closest living primate relatives: the chimpanzee. The use of  
50 biophysical models is crucial to tease apart and explain the neural basis of inter-species differences  
51 in whole-brain function, which cannot be achieved with current neuroimaging techniques [9]. By  
52 combining this innovative approach with a unique cross-species dataset, we reveal core neural  
53 principles likely to explain differences in brain function between humans and non-human primates.  
54

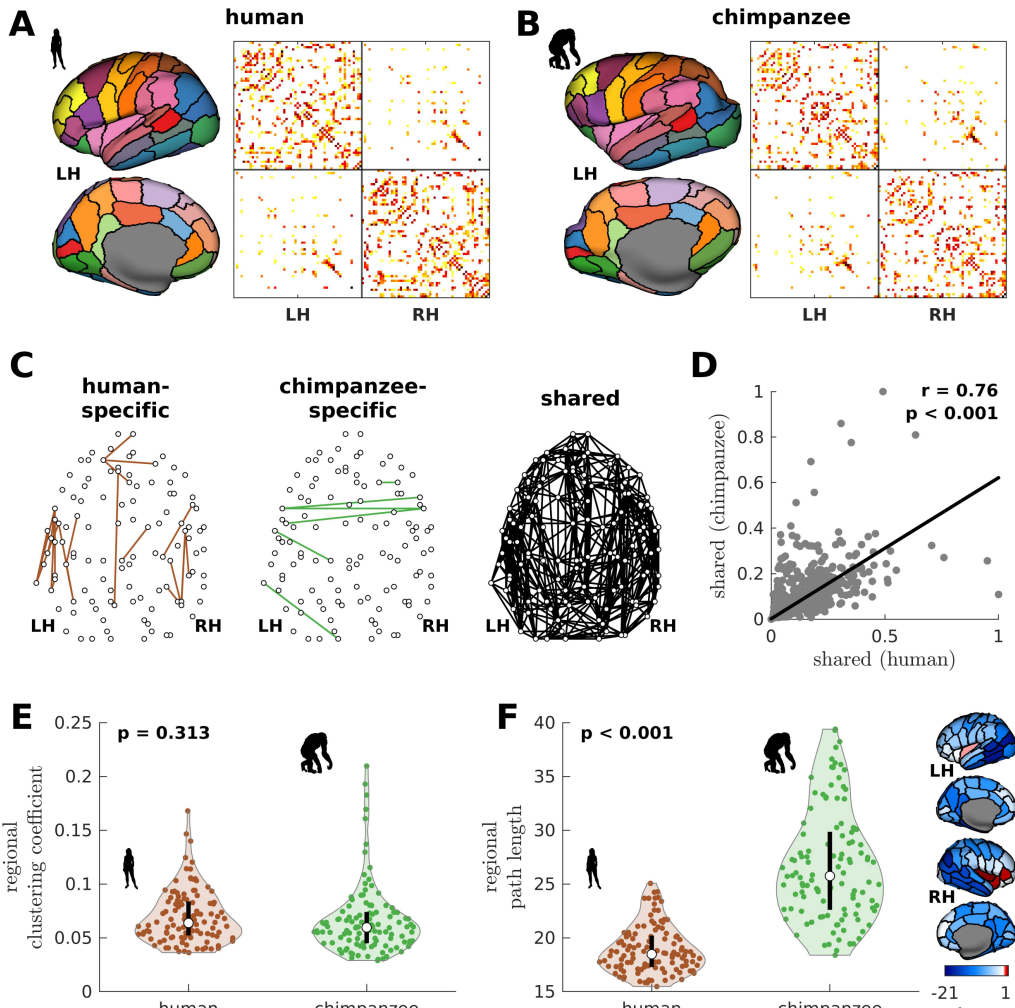
55 **RESULTS**

56 **Human and chimpanzee connectomes**

57 We begin by creating the connectomes of humans and chimpanzees. We use unique diffusion MRI  
58 data for adult humans (*Homo sapiens*) and sex-matched and age-equivalent chimpanzees (*Pan*  
59 *troglodytes*) to reconstruct the connectomes [7,10]. The connectomes represent cortico-cortical  
60 structural connections between 114 species-matched regions in both hemispheres (Table S1) from  
61 which we create group-averaged weighted human and chimpanzee connectomes [10] (Figs. 1A  
62 and 1B). We then normalize the group-averaged connectomes with respect to their maximum  
63 weights. Using the resulting connectomes, we examine connections present in one species but  
64 absent in the other (labeled as human-specific and chimpanzee-specific connections; Fig. 1C). We  
65 note that the use of the term “specific” does not necessarily imply that said connections are unique  
66 to each of the species; i.e., they are only specific based on comparison of the connectivity strength  
67 of connections between the two species in our dataset. We find that intrahemispheric pathways  
68 comprise 82.6% (19 out of 23) of human-specific connections and 50% (3 out of 6) of chimpanzee-  
69 specific connections, a finding consistent with previous comparative connectome investigations  
70 [7,10]. We also examine the set of connections that are present in both species, termed shared  
71 connections (Fig. 1C), and confirm that there is a strong correlation between connectivity strengths  
72 across both species (Fig. 1D), consistent with previous studies [7,10]. At the whole-brain level,  
73 the human and chimpanzee connectomes largely overlap in their topological organization. In  
74 particular, the connectomes show similar levels of small-worldness (small-world propensity [11]

75 values of 0.83 and 0.84 in human and chimpanzee, respectively) and modularity (modularity values of 0.54 and 0.56 in human and chimpanzee, respectively) [12,13]. At the regional level, the 76 connectomes exhibit similar distributions of clustering coefficients (Fig. 1E). On the other hand, 77 human brain regions have significantly shorter path lengths compared to chimpanzee brain regions 78 (Fig. 1F).  
79

80



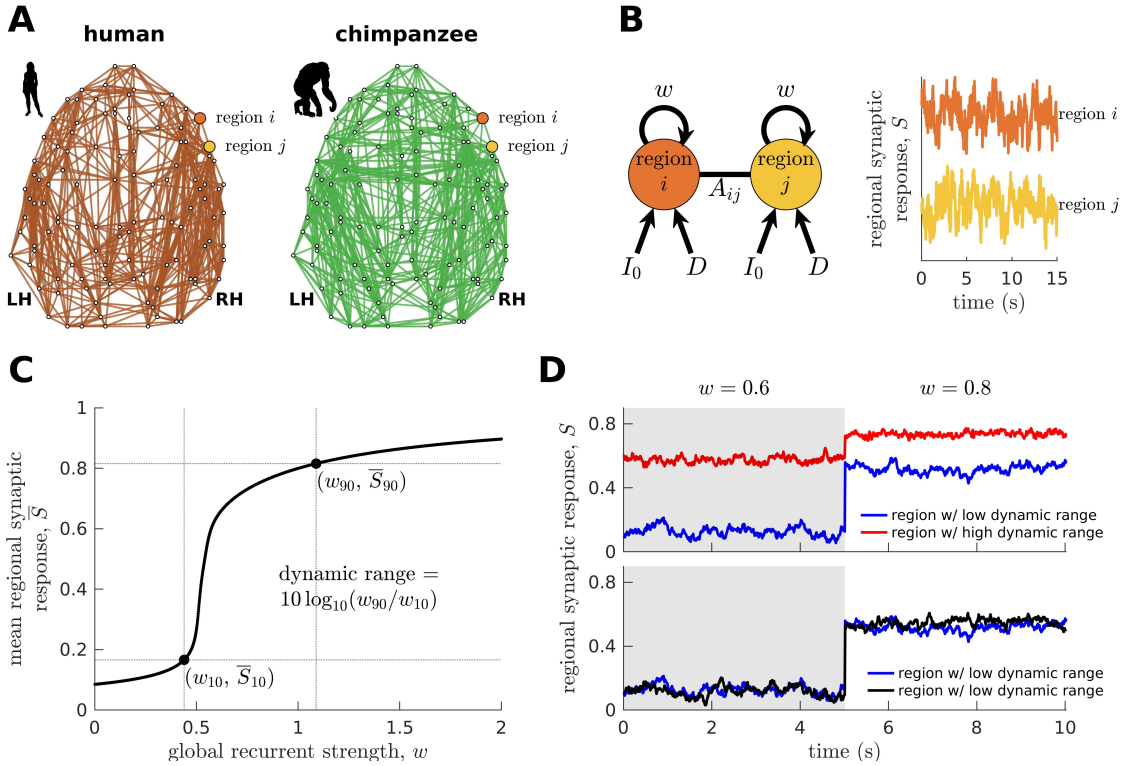
81  
82 **Fig. 1. Human and chimpanzee connectome properties.** (A–B) Parcellation and connectome. The surface  
83 plots show the 114-region atlas (Table S1) on inflated cortical surfaces. The matrices represent the group-  
84 averaged structural connectivity between brain regions. (C) Structural connections that are human-specific,  
85 chimpanzee-specific, and shared between humans and chimpanzees. (D) Association of the weights of the  
86 connections shared between humans and chimpanzees. The solid line represents a linear fit with Pearson's  
87 correlation coefficient ( $r$ ) and  $p$ -value ( $p$ ). (E) Violin plot of the distribution of regional clustering  
88 coefficients. Each violin shows the first to third quartile range (black line), median (white circle), raw data  
89 (dots), and kernel density estimate (outline).  $p$  is the  $p$ -value of the difference in the mean of the distribution  
90 between the species (two-sample t-test). (F) Violin plot of the distribution of regional path lengths. Violin  
91 plot details are similar to those in panel E. The surface plots show the spatial organization of the difference  
92 in path length between the species (i.e., human – chimpanzee) visualized on inflated human cortical  
93 surfaces. The negative-zero-positive values are colored as blue-white-red.  
94

95 **Modeling neural dynamics**

96 Next, we combine the connectomic data with a biophysical (generative) model [14–17] (Fig. 2B;  
97 see Materials and Methods) to generate regional synaptic response  $S$  across time (*neural dynamics*)  
98 specific to each species. The variable  $S$  represents the fraction of activated NMDA channels;  
99 hence, higher  $S$  values correspond to higher neural activity and firing rates. This model has been  
100 shown to reproduce empirical human functional neuroimaging data [16,17], which we confirmed  
101 (Fig. S1). Notably, we also confirmed the model's suitability to match non-human primate data  
102 (Fig. S1). These validations of the model on human and non-human primate data are important to  
103 ensure that the outcomes of the model capture meaningful properties of brain activity.

104 To understand how whole-brain activity patterns emerge, we analyze the intrinsic characteristics  
105 of regional neural dynamics. In particular, we determine a brain region's response function,  
106 describing the up- or downregulation of its mean activity following global (brain-wide)  
107 modulations in the strength of recurrent connections (Fig. 2C). This process can be linked to how  
108 structures in the ascending neuromodulatory systems (e.g., noradrenergic) facilitate the  
109 reorganization of cortex-wide dynamics by allowing coordinated communication between  
110 otherwise segregated systems [18–20]. In particular, previous work has shown that  
111 neuromodulatory agents can modify the biophysical properties of neurons through various cellular  
112 mechanisms [21]. One mechanism is via activation of metabotropic receptors that bring the resting  
113 membrane potential of neurons closer to their firing threshold [22]. This mechanism can mediate  
114 changes in the excitability of brain regions at the subsecond timescale [23], effectively driving  
115 modulations in the regional strength of recurrent connections (i.e., our model's  $w$  parameter).  
116 However, we clarify that the neuromodulation mechanism described above is only one example of  
117 many potential mechanisms that can drive changes in regional excitability.

118 We characterize the shape of the response function (i.e., the slope) demonstrated in Fig. 2C in  
119 terms of the *neural dynamic range*, such that high dynamic range means that a region can respond  
120 to a wide range of changes in excitability ( $w$ ), albeit the transition between activity levels is slow  
121 (red curve in the top panel of Fig. 2D). Conversely, regions with a low dynamic range can quickly  
122 transition to high levels of activity with small changes in excitability, specifically at a critical  
123 intermediate regime (blue curve in the top panel of Fig. 2D). When the dynamic range is very close  
124 to zero, the response function in Fig. 2C becomes like a step function with infinite slope; hence,  
125 the response jumps between low and high activity levels, analogous to a phase transition. Note that  
126 our dynamic range is based on an excitability-output function (Fig. 2C) rather than an input  
127 stimulus-output function commonly used in previous studies [24]. Moreover, our definition of  
128 dynamic range is different from other definitions based on temporal deviations of a signal with  
129 respect to its mean [25]. Brain regions with similarly low or high dynamic ranges are more likely  
130 to reach equivalent functional states. This can be observed in the example time series at the bottom  
131 panel of Fig. 2D, where regions with similarly low dynamic ranges have activity amplitudes  
132 fluctuating at similar levels across varying excitability regimes. Note that similar observations  
133 occur for regions with similarly high dynamic ranges. Moreover, regions with similar dynamic  
134 ranges have higher levels of correlated activity compared to regions with different dynamic ranges,  
135 suggesting better integration (e.g., see correlations of the time series in the bottom versus top  
136 panels of Fig. 2D at corresponding  $w$  values). Using the neural dynamic range property, we aim  
137 to reveal key principles of whole-brain neural dynamics setting humans apart from other species.



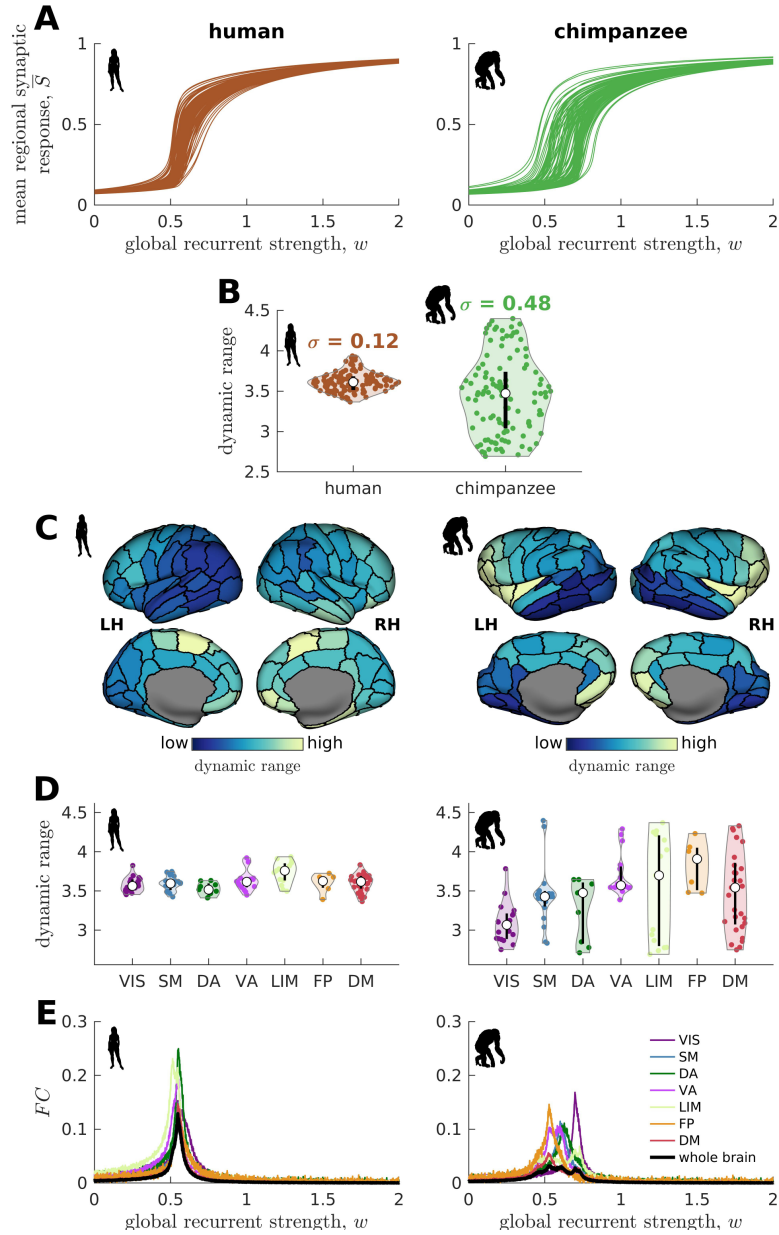
139

140 **Fig. 2. Brain network modeling.** (A) Group-averaged human and chimpanzee networks visualized on the  
 141 same brain template. Top 20% of connections by strength are shown. (B) Schematic diagram of the model.  
 142 Each brain region is recurrently connected with strength  $w$  and driven by an excitatory input  $I_0$  and white  
 143 noise with standard deviation  $D$ . The connection between regions  $i$  and  $j$  is weighted by  $A_{ij}$  based on the  
 144 connectomic data. The regional neural dynamics are represented by the synaptic response variable  $S$ ; high  
 145  $S$  translates to high neural activity. (C) Method for calculating the dynamic range of each brain region from  
 146 its mean synaptic response  $\bar{S}$  versus global recurrent strength  $w$  curve. Note that  $\bar{S}_x = \bar{S}_{\min} + (x/100) * (S_{\max} - S_{\min})$ ,  
 147 with  $w_x$  being the corresponding global recurrent strength at  $\bar{S}_x$  and  $x = \{10, 90\}$ . (D)  
 148 Example time series of regions with different (top panel) and similar (bottom panel) dynamic ranges at  $w = 0.6$   
 149 and  $w = 0.8$ . The time series in the top panel have correlation values (Pearson's  $r$ ) of 0.06 and 0.08 at  $w = 0.6$  and  $w = 0.8$ , respectively. The time series in the bottom panel have correlations of 0.40 and 0.14 at  $w = 0.6$  and  $w = 0.8$ , respectively.

### 152 Human brains have more constrained neural dynamics than chimpanzee brains

153 We find that the response functions of human brain regions (reflecting how activity changes versus  
 154 modulations in global excitability) are more similar to one another compared to those of  
 155 chimpanzees (Fig. 3A). We quantitatively test this observation by calculating the distribution of  
 156 dynamic ranges across regions (Fig. 3B). The results show that the human brain has neural  
 157 dynamic ranges characterized by a narrower distribution (standard deviation  $\sigma = 0.12$ ) as compared  
 158 to the chimpanzee brain ( $\sigma = 0.48$ ). This finding is robust against differences in individual-specific  
 159 connectomes (Figs. S2A and S2B), brain volume (Fig. S2C), connection density (Fig. S3), inter-  
 160 individual variability of connection strengths (Fig. S4), data sample size (Fig. S5), propagation  
 161 delays between brain regions (Fig. S6), and heterogeneous excitatory input across brain regions  
 162 (Fig. S7). Moreover, our results are replicated on independent human data from the Human  
 163 Connectome Project [26] (Fig. S8) and a different computational model (Fig. S9).

164

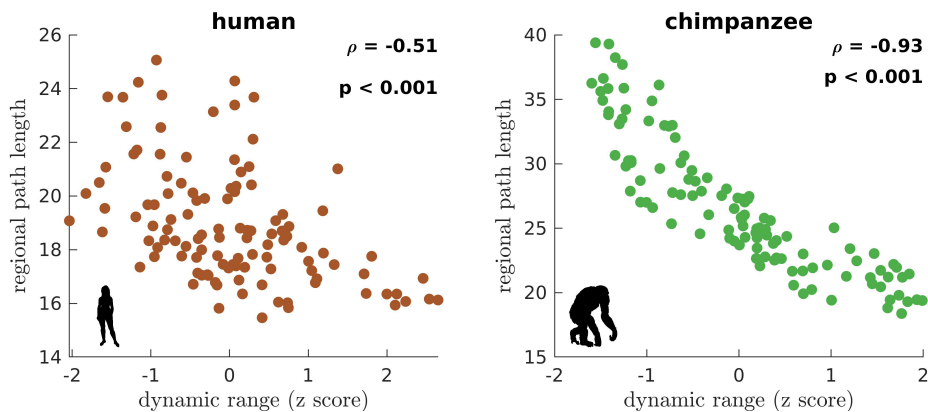


165

166 **Fig. 3. Human and chimpanzee neural dynamics.** (A) Regional neural dynamics as a function of global  
 167 recurrent strength ( $w$ ). (B) Violin plot of the distribution of dynamic ranges across brain regions. Each  
 168 violin shows the first to third quartile range (black line), median (white circle), raw data (dots), and kernel  
 169 density estimate (outline).  $\sigma$  is the standard deviation of the distribution. (C) Spatial organization of  
 170 dynamic ranges. Data are visualized on inflated cortical surfaces. Light color represents high dynamic range  
 171 and dark color represents low dynamic range. (D) Violin plot of the distribution of dynamic ranges in 7  
 172 canonical brain networks. Violin plot details are similar to those in panel B. (E) Simulated average  
 173 functional connectivity ( $FC$ ) within the networks in panel D as a function of  $w$ . The black line represents  
 174 the average  $FC$  across the whole brain.  
 175

176 **Neural dynamic range is spatially organized along the anterior-posterior brain axis**  
 177 When we map the dynamic ranges onto the anatomical locations of each brain region, we find that  
 178 both species follow a dominant gradient of neural dynamic ranges spatially organized along the  
 179 anterior-posterior axis (Fig. 3C). Specifically, anterior brain regions show neural dynamics with  
 180 higher dynamic ranges, while posterior regions have lower dynamic ranges. Interestingly, we  
 181 observe that this dominant gradient is more prominent in chimpanzees than in humans (Fig. S10A).  
 182 A similar anterior-posterior gradient has also been found in empirical evolutionary expansion maps  
 183 of the human cortex [27], with frontal regions being more expanded in humans compared to  
 184 chimpanzees [3,4] and the occipital cortex having relatively similar sizes across the two species  
 185 (Fig. S10B). Taken together, we additionally observe that highly expanded anterior regions have  
 186 higher dynamic ranges compared to lowly expanded posterior regions (Fig. S10C).

187 **Similar neural dynamic ranges across regions enables brain network integration**  
 188 We next ask whether brain regions belonging to specific functional networks have neural dynamics  
 189 with similar levels of dynamic range. We cluster brain regions into 7 common large-scale brain  
 190 networks according to [27,28]: Visual (VIS), Somatomotor (SM), Dorsal-Attention (DA), Ventral-  
 191 Attention (VA, also known as the Salience network), Limbic (LIM), Frontoparietal (FP), and  
 192 Default-Mode (DM) networks (Fig. S11). These networks represent functionally coupled regions  
 193 across the cerebral cortex. In humans, brain regions belonging to each functional network show  
 194 relatively similar neural dynamic ranges (Fig. 3D). Conversely, in chimpanzees, neural dynamic  
 195 ranges follow a marked functional hierarchy with cognitive networks (i.e., VA, LIM, FP, DM)  
 196 having higher median values than sensory networks (i.e., VIS, SM, DA). Furthermore, the patterns  
 197 of within-network changes in functional connectivity versus modulations in global excitability  
 198 overlap strongly in humans but not in chimpanzees (Fig. 3E). Thus, similar levels of regional  
 199 dynamic ranges allow the human brain to better integrate activity within functionally specialized  
 200 brain networks (colored lines in Fig. 3E) and the whole brain (black line in Fig. 3E). This finding  
 201 is consistent with the higher level of structural integration imposed by the human connectome, as  
 202 quantified by lower topological path length (Fig. 1F). Moreover, we find that the heterogeneity in  
 203 regional path lengths could explain the heterogeneity in neural dynamics, where regions with  
 204 shorter paths (i.e., lower path length values reflecting higher ability to integrate information  
 205 between regions) tend to have higher dynamic ranges (Fig. 4).  
 206

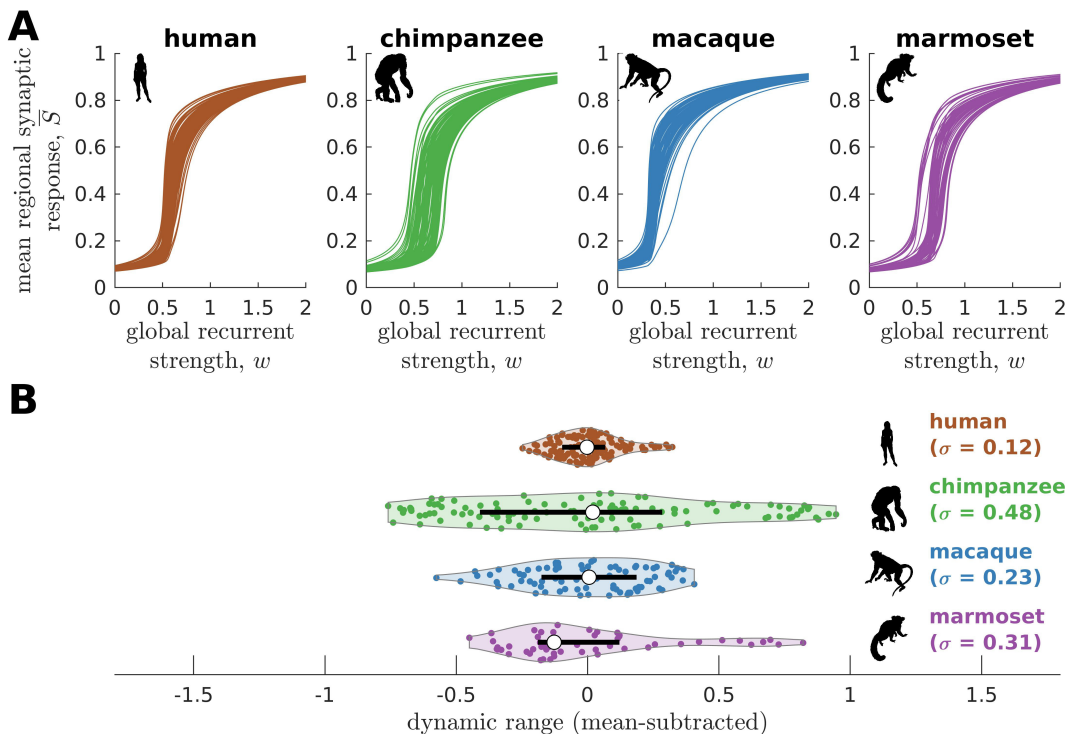


207  
 208 **Fig. 4. Association of the human and chimpanzee connectomes' path length and dynamic range.**  
 209 Average regional path length as a function of z-score-transformed dynamic ranges.  $\rho$  is the Spearman rank  
 210 correlation and  $p$  is the p-value.  
 211

212 **Neural dynamic range differentiates humans and non-human primates**

213 To further test the hypothesis that neural dynamic range is a key feature setting the human brain  
 214 apart from the brains of other species, we perform similar analyses on other non-human primate  
 215 connectomic data: macaque (*Macaca mulatta*) [29] and marmoset (*Callithrix jacchus*) [30]. Neural  
 216 dynamics are obtained via the model in Fig. 2B and using weighted connectomes generated from  
 217 diffusion MRI (for macaques) and invasive tract tracing (for marmosets). The connectomes  
 218 represent connections between 82 and 55 regions of the macaque and marmoset brains,  
 219 respectively. Both species have neural response functions and dynamic ranges closer to  
 220 chimpanzees than to humans (Fig. 5;  $\sigma = 0.23$  for macaque and  $\sigma = 0.31$  for marmoset), further  
 221 validating our results in Fig. 3 across species and across methodological differences in connectome  
 222 data type and resolution. To verify that the macaque results are not driven by one apparent outlier,  
 223 as seen in Fig. 5A, we perform the analysis on independent macaque dataset and find that the  
 224 results are replicated (Fig. S12).

225



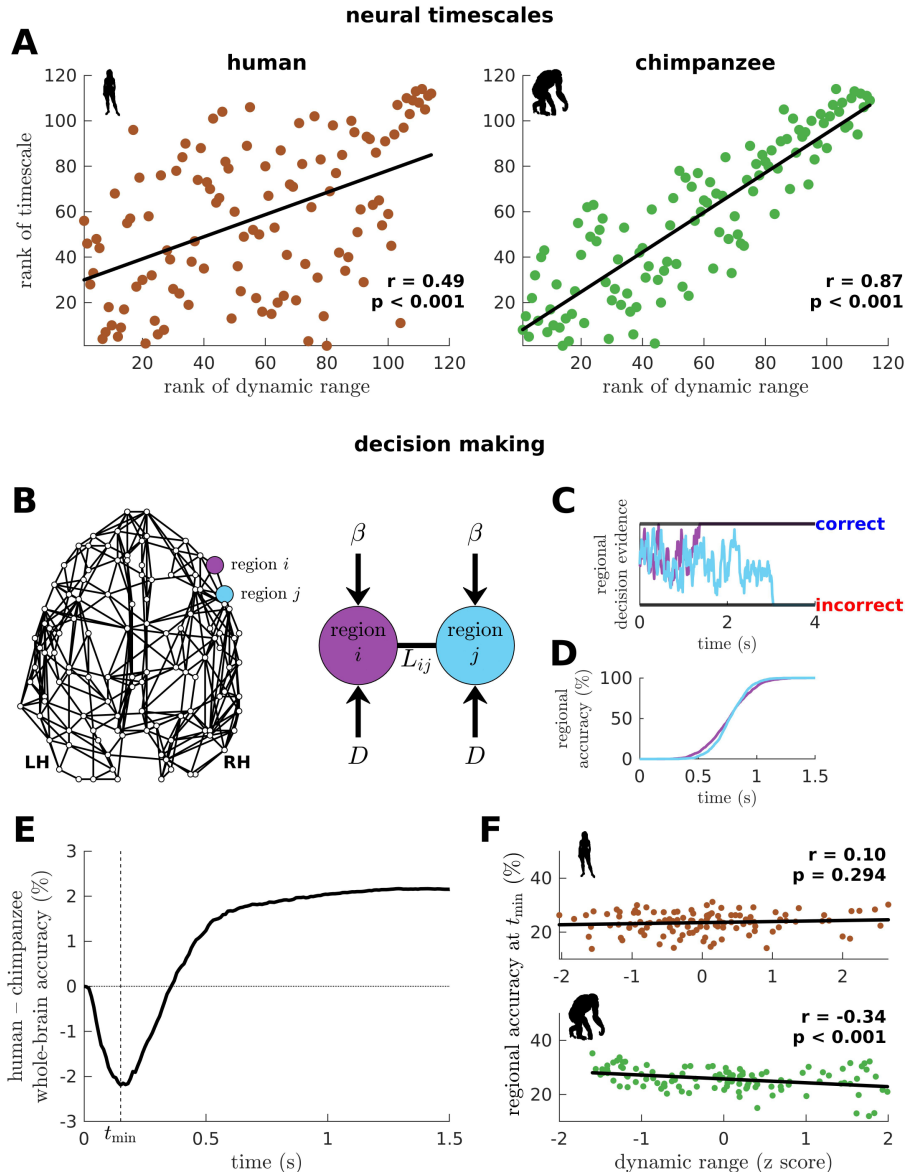
226

227 **Fig. 5. Neural dynamics of human and non-human primates.** (A) Regional neural dynamics as a  
 228 function of global recurrent strength ( $w$ ) for human, chimpanzee, macaque, and marmoset. (B) Violin plot  
 229 of the distribution of dynamic ranges across brain regions. Violin plot details are similar to those in Fig.  
 230 3B. The data are mean-subtracted for visual purposes.  $\sigma$  is the standard deviation of the distribution.

231 **Neural dynamic range is linked to the temporal structure of brain activity**

232 To this point, we have shown that the human connectome supports neural dynamics with a  
 233 narrower distribution of dynamic ranges than the chimpanzee connectome (as well as other non-  
 234 human primates). However, it remains unclear how dynamic range relates to the temporal structure  
 235 of neural activity across the brain. Studies have shown that activity within brain regions exhibits a  
 236 cortex-wide hierarchy of intrinsic neural timescales [31–33]. From these findings, we examine  
 237 whether a brain region's neural timescale may be related to its neural dynamic range. We extract

238 the timescale by fitting the autocorrelation of the simulated neural activity with a single  
 239 exponential decay (Fig. S13; see Materials and Methods). We find that regional neural timescales  
 240 (ranges: 0.12–0.24 s for humans and 0.12–0.55 s for chimpanzees) are significantly correlated with  
 241 dynamic ranges, and this relation is stronger in chimpanzees (Fig. 6A; this finding also holds for  
 242 macaques and marmosets as shown in Fig. S14A). This result is consistent with the examples in  
 243 Fig. 2D, such that the fast neural timescale of a region with a low dynamic range accommodates  
 244 the quick transition in response amplitudes of that region when the excitability is increased.



245

246 **Fig. 6. Human and chimpanzee neural timescales and connectome decision-making capacity.** (A)  
 247 Ranked neural timescales as a function of ranked dynamic ranges. The solid line represents a linear fit with  
 248 Pearson's correlation coefficient ( $r$ ) and  $p$ -value ( $p$ ). (B) Exemplar connectome and schematic diagram of  
 249 the drift-diffusion model. In the model, each brain region accumulates decision evidence via a diffusion  
 250 (Brownian) process with drift rate  $\beta$  and driving white noise with standard deviation  $D$ . Regions  $i$  and  $j$  are  
 251 connected with Laplacian weight  $L_{ij}$  based on the connectomic data. (C) Example time series of regional

252 decision evidence across time for regions  $i$  and  $j$ , demonstrating how each region reaches a correct or  
253 incorrect decision. (D) Regional accuracy curves obtained by simulating the model for an ensemble of trials  
254 and calculating the rate of achieving the correct decision. (E) Difference in whole-brain accuracy across  
255 time between humans and chimpanzees. Whole-brain accuracy represents the average of the accuracy of  
256 all regions. The dashed line shows the time ( $t_{\min}$ ) at which the difference in accuracy between humans and  
257 chimpanzees is most negative (i.e., chimpanzee accuracy > human accuracy). (F) Regional accuracy at  $t_{\min}$   
258 (found in panel E) as a function of z-score-transformed dynamic ranges. The solid line represents a linear  
259 fit with Pearson's correlation coefficient (r) and p-value (p).

260 **Neural dynamic range affects the decision-making capacity of human and chimpanzee**  
261 **connectomes**

262 We next ask what would be the implication of the differences in dynamic range distributions  
263 between humans and chimpanzees in terms of brain function. We hypothesize that these  
264 differences will likely impact the facilitation of whole-brain integration of neural processes, which  
265 has been found to be important for performing sensory-perceptual [34] and complex cognitive  
266 tasks [18] in humans. Note, however, that current whole-brain neuroimaging techniques cannot  
267 yet capture the direct effects of neural dynamic range on task performance. Moreover, new  
268 chimpanzee brain data via imaging or invasive recordings are not possible to be acquired for ethical  
269 reasons.

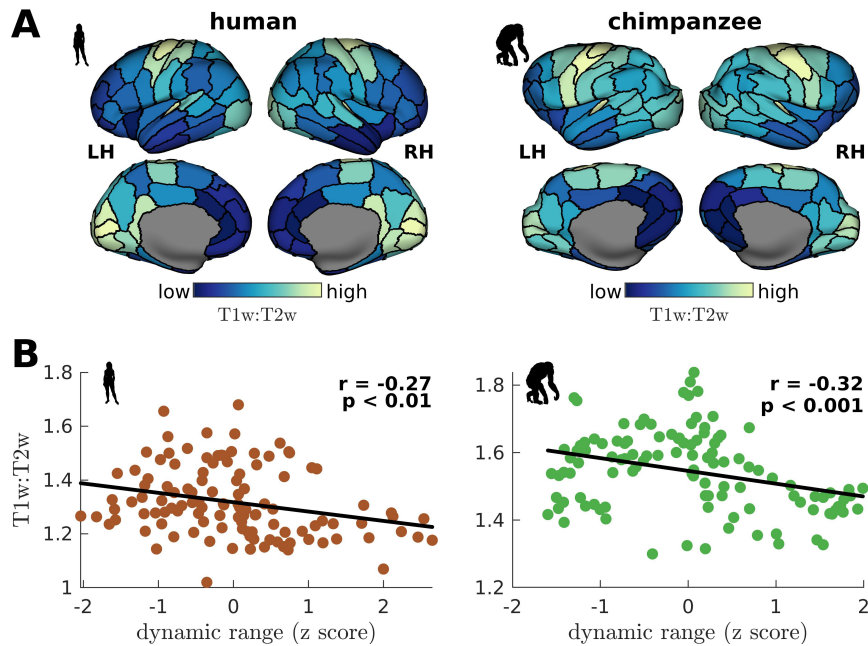
270 To provide insights into our question, we adopt a computational drift-diffusion model [35] (Fig.  
271 6B), which is widely used to predict behavioral responses of both humans and animals performing  
272 tasks such as decision making. This model allows us to quantify the capacity of a brain region to  
273 achieve a decision threshold by integrating the evidence accumulated by its nearest neighbors.  
274 Here, we use the human and chimpanzee connectomes to define a region's neighborhood. The  
275 model calculates the accumulation of evidence through time in each brain region via a noise-driven  
276 diffusion process until a set threshold is reached (Fig. 6C; there are two possible thresholds  
277 corresponding to a correct or incorrect decision). Then, we estimate each brain region's accuracy  
278 in reaching a correct choice across an ensemble of trials (Fig. 6D) and average these values,  
279 representing the likely decision accuracy of the whole brain. Note that we adopt a generalized  
280 definition of decision accuracy based on the performance of the connectomes. Specifically, we do  
281 not take into account the possibility that only a subset of brain regions are recruited in the decision-  
282 making process. At the end of our simulation, the human brain has a higher accuracy in achieving  
283 the correct choice compared to the chimpanzee brain (Fig. 6E; this finding also holds for macaques  
284 and marmosets as shown in Fig. S14B). Interestingly, we find that at earlier times ( $t < 0.36$  s), the  
285 decision accuracy of the human brain is lower than the chimpanzee counterpart. This finding is  
286 driven by regions in the chimpanzee brain with low dynamic ranges that can reach correct  
287 decisions quickly (Fig. 6F).

288 We next investigate whether levels of excitation and inhibition could have also influenced the  
289 difference between the decision accuracy of human and chimpanzee brains at earlier times (Fig.  
290 6E). Hence, we extend the drift-diffusion model in Fig. 6B by incorporating a self-coupling term  
291 parametrized by  $\lambda$  (Fig. S15A;  $\lambda > 0$  and  $\lambda < 0$  corresponds to increased excitation and inhibition,  
292 respectively) [36,37]. We find that increased excitation leads to faster decision times (Fig. S15B)  
293 but poorer overall decision accuracy (Fig. S15C). We also find that increased inhibition extends  
294 periods of inferior whole-brain decision accuracy of the human brain compared to the chimpanzee  
295 brain at earlier times (Fig. S15D). Interestingly, we also find that the human brain requires  
296 additional level of excitation (i.e.,  $\lambda = 2.03$ ) at earlier times in order to reach the level of decision

accuracy achieved by the chimpanzee brain (Fig. S15E). This result suggests that our original finding in Fig. 6E could also be driven by higher intrinsic levels of inhibition in the human brain.

## Testing of model predictions on empirical data

We have shown that a brain region's neural dynamic range is tightly linked to the temporal structure of its activity (i.e., neural timescale), suggesting a role of dynamic range in local processing speeds. To test this prediction, we compare empirical cortical T1w:T2w maps, which is an MRI contrast sensitive to myelination, of humans and chimpanzees [38] (Fig. 7A) to each region's dynamic range. T1w:T2w myelination maps have been shown to be a good macroscale proxy of the cortical processing hierarchy in humans and non-human primates [38–40], where unimodal sensory-motor regions tend to be highly myelinated and transmodal regions lightly myelinated. Crucially, myelination has been found to be tightly coupled with electrophysiological measures of a region's temporal processing speed [32]. Accordingly, we find that myelination is inversely related with neural dynamic range (Fig. 7B). The inverse relation of dynamic range and T1w:T2w is consistent with other studies [25], although their dynamic range metric quantifies the diversity in the fluctuations of activity amplitudes. This result provides an empirical neurobiological support to our findings in Fig. 6A, demonstrating that dynamic range is related to a region's processing speed.

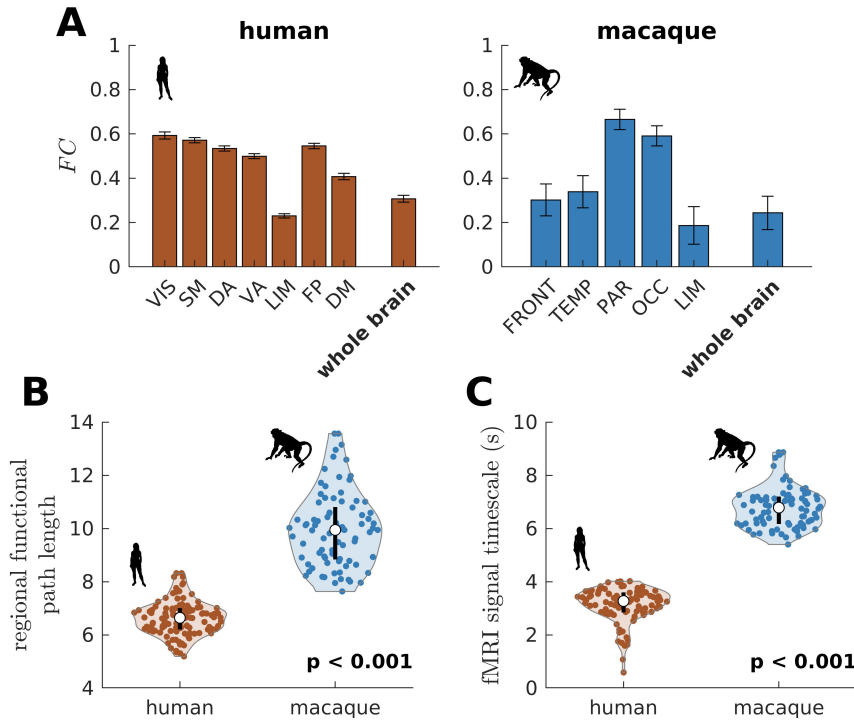


314

**Fig. 7. Testing of model predictions on T1w:T2w data.** (A) T1w:T2w maps visualized on inflated cortical surfaces. Light color represents high T1w:T2w value (high myelination) and dark color represents T1w:T2w value (low myelination). (B) Regional T1w:T2w as a function of z-score-transformed dynamic ranges. The solid line represents a linear fit with Pearson's correlation coefficient ( $r$ ) and p-value ( $p$ ).

315 We have also shown that the more constrained neural dynamics of the human brain compared to  
316 the chimpanzee brain allows better integration of whole-brain activity. We test this prediction on  
317 empirical neuroimaging (i.e., fMRI) data. Because we do not have access to chimpanzee fMRI  
318 data, we compare human with macaque data (the same data used in Fig. S1 to validate our model's  
319 suitability). As predicted, we find that functional connectivity (*FC*) within large-scale networks is

generally higher and more homogeneous in humans compared to macaques (Fig. 8A). The human brain also has higher between network functional connectivity, as demonstrated by a higher whole-brain *FC* ( $p < 0.001$ ). Moreover, the human brain has shorter functional paths (i.e., lower path length values) than the macaque brain (Fig. 8B; similar metric used in Fig. 1F but applied here on functional connectivity matrices), which corresponds to better functional integration. We also estimated regional timescales by applying the same technique described in Fig. S13 on fMRI signals, finding that the human brain has faster timescales than the macaque brain (Fig. 8C). Overall, we have used available empirical human and non-human primate neuroimaging data to validate two key predictions of our model: neural dynamic range is linked to local processing speed and a narrower dynamic range distribution in humans allows better integration of whole-brain activity.



335

**Fig. 8. Testing of model predictions on functional neuroimaging data.** (A) Functional connectivity (*FC*) within large-scale networks and across the whole brain of humans and macaques. The human large-scale networks are similar to those defined in Fig. 1F. The macaque large-scale networks are: FRONT = Frontal; TEMP = Temporal; PAR = Parietal; OCC = Occipital; LIM = Limbic. The error bars are standard errors of the mean across subjects. (B) Violin plot of the distribution of regional functional path length across brain regions calculated from group-averaged functional connectivity matrices. Violin plot details are similar to those in Fig. 3B. (C) Violin plot of the distribution of fMRI signal timescales. Violin plot details are similar to those in Fig. 3B. For panels B and C, *p* is the *p*-value of the difference in the mean of the distribution between the species (two sample t-test).

## 345 DISCUSSION

346 There is converging evidence that the human brain, as compared to that of our primate relatives,  
347 has experienced significant structural reorganizations in association regions throughout evolution  
348 [3,41]. Here, we took advantage of a unique neuroimaging dataset of sex-matched and age-  
349 equivalent human and chimpanzee to study how the structural brain wirings of these species

350 support different patterns of whole-brain neural dynamics underpinning brain function. Our results  
351 show that these differences determine how the activities of segregated regions are integrated across  
352 the brain, giving rise to distinct computational capacities of humans and chimpanzees.

353 For each species, we determined their brain regions' response functions, which describe the  
354 regulation of intrinsic neural activity following brain-wide modulations in excitability.  
355 Modulations in global excitability could come from various sources, from external inputs [42] to  
356 internal influences such as neuromodulation [19,20,23]. The response function of each region  
357 encapsulates all these phenomena, differentiating it from typical input-output response curves  
358 [24,43], with its shape, particularly its slope, characterized by the neural dynamic range. A high  
359 dynamic range means that a region can slowly change its activity in response to a wide range of  
360 modulations in excitability. Conversely, a low dynamic range means that a region can quickly  
361 transition between low and high levels of activity within a narrow range of changes in excitability.  
362 We reasoned that the up or down regulation of local neural activity is crucial to facilitate  
363 communication across brain regions, enabling large-scale functional integration and related  
364 computations.

365 In humans, brain regions showed response functions that were more similar to one another than  
366 their chimpanzee counterparts. Moreover, the distribution of neural dynamic ranges in humans  
367 was narrower than that in chimpanzees and in other non-human primate species (i.e., macaques  
368 and marmosets). Thus, neural dynamic range seems to be a unifying feature that sets human brains  
369 apart from other primate species. Note, however, that the generalization of the relationship  
370 between dynamic range and the evolutionary trajectory of non-human primates is beyond the scope  
371 of the current study and remains to be established. These results also propose the hypothesis that  
372 relatively subtle evolutionary differences in the connectomes of humans and chimpanzees [8] have  
373 a marked impact on large-scale neural dynamics supporting the ability of the brain to process  
374 information. This could be why human-specific features of connectome organization are  
375 vulnerable to brain dysfunction [10,44].

376 It has recently been shown that the structural, functional, and genetic properties of cortical regions  
377 are spatiotemporally organized in a hierarchical manner [33,40,45–49]. Accordingly, we found  
378 that neural dynamic ranges follow a dominant spatial gradient along the anterior-posterior brain  
379 axis, with anterior associative regions having higher dynamic ranges than posterior sensory  
380 regions. This spatial gradient mirrors the cytoarchitectonic (e.g., cell density) organization  
381 observed in the brains of several mammalian species, including rodents and primates [50–52]. By  
382 analyzing the intrinsic timescales of fluctuations of neural activity [31–33], we showed that  
383 regional neural dynamic ranges correlated with regional neural timescales. Thus, dynamic range  
384 seems to capture local information processing speed, providing support to our prior hypothesis that  
385 brain regions with similar dynamic ranges are more likely to reach equivalent functional states due  
386 to similar processing capacity. At the level of large-scale networks, chimpanzees showed a marked  
387 functional hierarchy in neural dynamic ranges compared to humans, with unimodal sensory-  
388 perceptual networks having lower values than transmodal associative networks. Importantly, this  
389 more pronounced hierarchy in dynamic ranges limits brain network integration in chimpanzees  
390 compared to humans. Human brain connectivity appears therefore to have evolved to support  
391 neural dynamics that maintain relatively high levels of integration between functionally segregated  
392 brain systems [7,8].

393 By using a computational drift-diffusion model [35], we assessed the functional consequences of  
394 neural dynamic range to the human and chimpanzee connectomes' decision-making capacity. Over

395 relatively long processing periods, the human connectome had a higher accuracy in achieving a  
396 correct choice compared to the chimpanzee connectome. However, over short periods of  
397 processing time, the human connectome performed worse than the chimpanzee counterpart. This  
398 latter result was attributed to the (i) more heterogeneous distribution of dynamic ranges in  
399 chimpanzees, supporting that diversity in local neural properties is important for rapid  
400 computations [43], and (ii) higher intrinsic levels of inhibition in the human brain [36,37]. This  
401 regional diversity and higher intrinsic inhibition may explain why chimpanzees are able to perform  
402 at least as well as, or better than, humans in simple sensory-motor tasks [53]. Moreover, our  
403 findings provide a possible neural mechanism for why humans generally outperform chimpanzees  
404 in tasks requiring longer computational processing [54,55]. In line with our results, studies have  
405 suggested that behavioral differences between humans and chimpanzees are more prominent in  
406 complex tasks involving intersubjectivity (e.g., theory of mind [56]). This important brain capacity  
407 is known to be supported by the activity of the Default-Mode Network (DMN) [57,58], which  
408 displays significant genetic, anatomical, and functional differences between humans and non-  
409 human primates [27,59,60]. By making use of our simulations assessing decision-making capacity,  
410 we found that the accuracy of DMN for relatively long computations was more accurate in humans  
411 compared to chimpanzees (Fig. S16). This finding further suggests that the DMN may be critical  
412 in differentiating the functions of human and chimpanzee brains.

413 Results from the current study suggest that evolution has shaped the human brain to optimize fast  
414 transmodal integration of neural activity across brain regions supporting complex functions  
415 including social-cultural skills [48,61]. While our results are consistent with the hypothesis that  
416 the human brain has evolved to facilitate rapid associative computations [56], they also highlight  
417 that this evolutionary adaptation may hinder rapid processing within functionally specialized  
418 systems. The unique properties of human and chimpanzee brain dynamics may therefore be  
419 understood as an evolutionary tradeoff between functional segregation and integration.  
420 Collectively, our findings inform on the likely neural principles governing evolutionary shifts that  
421 could explain the differences in brain function between humans and our closest primate relatives  
422 [62]. Moreover, our work provides a framework to investigate the relationship between whole-  
423 brain connectivity and neural dynamics across a wider family of species (e.g., across the  
424 mammalian species [63]) and its effects on complex cognitive processes (e.g., decision making  
425 with more than two alternatives [64]).

426

## 427 MATERIALS AND METHODS

### 428 Connectomic data

429 *Human and chimpanzee.* Diffusion MRI data for 58 humans (*Homo sapiens*,  $42.5 \pm 9.8$  years,  
430 female) and 22 chimpanzees (*Pan troglodytes*,  $29.4 \pm 12.8$  years, female) were taken from previous  
431 studies [7,10]. Procedures were carried out in accordance with protocols approved by the Yerkes  
432 National Primate Research Center and the Emory University Institutional Animal Care and Use  
433 Committee (YER-2001206). All humans were recruited as healthy volunteers with no known  
434 neurological conditions and provided informed consent (IRB00000028). We only provide below  
435 a brief account of details of the data and we refer the readers to previous studies for further details.  
436 The diffusion MRI acquisition parameters for humans were: spin-echo echo planar imaging (EPI),  
437 isotropic voxel size of 2 mm, b-weighting of  $1000 \text{ s/mm}^2$ , 8 b<sub>0</sub>-scans, and scan time of 20 mins.  
438 For chimpanzees: spin-echo EPI, isotropic voxel size of 1.8 mm, b-weighting of  $1000 \text{ s/mm}^2$ , 40  
439 b<sub>0</sub>-scans, and scan time of 60 mins. The acquired data were then preprocessed to correct for eddy-

440 current, motion, susceptibility, and head motion distortions. Each participant's cortex was then  
441 parcellated using a 114-area subdivision of the Desikan-Killiany atlas [65] (Table S1). Individual  
442 undirected connectome matrices were constructed via deterministic tractography to establish  
443 cortico-cortical connections between the 114 regions. In line with previous research [10], we  
444 removed idiosyncratic variations by taking the average weight across individuals of each  
445 connection that was consistently found in  $\geq 60\%$  of the individuals, resulting in a group-averaged  
446 weighted connectome for each species.

447 *Macaque*. The whole-brain macaque (*Macaca mulatta*) connectome was derived from 8 adult  
448 males using diffusion MRI. The data were taken from an open-source dataset, which provides in-  
449 depth description of the data [29]. In brief, the diffusion MRI acquisition parameters were: 2D  
450 EPI, isotropic voxel size of 1 mm, b-weighting of 1000 s/mm<sup>2</sup>, 64 directions, and 24 slices. The  
451 acquired data were then preprocessed to correct image distortion and to model fiber directions.  
452 Each macaque's cortex was then parcellated into 82 regions following the Regional Map (RM)  
453 atlas [66]. Individual directed connectome matrices were constructed via probabilistic tractography  
454 to establish connections between the 82 regions and thresholded to remove weak connections  
455 (thresholds of 0% to 35%; see [29] for specific optimal threshold values used per individual). A  
456 group-averaged weighted connectome was obtained by taking the average weight of non-zero  
457 elements of the connectome matrices. It was then thresholded to match the connection density of  
458 the group-averaged chimpanzee connectome.

459 *Marmoset*. The marmoset (*Callithrix jacchus*) connectome data were downloaded from the  
460 Marmoset Brain Connectivity atlas (marmosetbrain.org) [30], which is a publicly available  
461 repository of cellular resolution cortico-cortical connectivity derived from neuroanatomical  
462 tracers. In brief, the connectome was reconstructed from 143 injections of six types of retrograde  
463 fluorescent tracers performed on 52 young adult marmosets (1.4–4.6 years, 21 females).  
464 Connection weights represent the fraction of labeled neurons found in the target area with respect  
465 to the total number of labeled neurons excluding the neurons in the injected area. The connections  
466 were projected onto the Paxinos stereotaxic atlas [67], comprising 116 cortical areas. Individual  
467 directed connectome matrices were constructed by including only areas with pairwise-complete  
468 connection values. Thus, the final connectome matrices were  $55 \times 55$  in size. A group-averaged  
469 weighted connectome was obtained by taking the average weight of non-zero elements of the  
470 connectome matrices. It was then thresholded to match the connection density of the group-  
471 averaged chimpanzee connectome.

472 *Human HCP*. For replication of human results (Fig. S8), minimally preprocessed diffusion MRI  
473 data from 100 unrelated healthy young adult participants ( $29.1 \pm 3.7$  years, 54 females) were  
474 obtained from the Human Connectome Project (HCP) [26]. In brief, the diffusion MRI acquisition  
475 parameters were: isotropic voxel size of 1.25 mm, TR of 5520 ms, TE of 89.5 ms, b-weightings of  
476 1000, 2000, and 3000 s/mm<sup>2</sup>, and 174 slices. The data were then preprocessed for bias-field  
477 correction and multi-shell multi-tissue constrained spherical deconvolution to model white matter,  
478 gray matter, and cerebrospinal fluid using the MRtrix software [68]. For each participant,  
479 tractograms were generated using 100 million probabilistic streamlines, anatomically-constrained  
480 tractography (ACT) [69], the 2<sup>nd</sup>-order Integration over Fiber Orientation Distributions algorithm  
481 (iFOD2), dynamic seeding [70], backtracking, streamline lengths of 5–250 mm, and spherical-  
482 deconvolution informed filtering of tractograms (SIFT2). Each participant's tractogram was  
483 projected onto the cortex that was parcellated into 100 regions following the Schaefer atlas [71] to  
484 obtain the connectome matrices. A group-averaged weighted connectome was obtained by taking

485 the average weight of non-zero elements of the connectome matrices. It was then thresholded to  
486 match the connection density of the chimpanzee connectome.

487 *Macaque (CoCoMac)*. For replication of macaque results (Fig. S12), a directed binary connectome  
488 was taken from an open-source dataset (the CoCoMac database) [72,73]. The connectome  
489 represents cortico-cortical structural connections between 71 regions derived from histological  
490 tract tracing studies.

#### 491 **fMRI data**

492 *Human*. The empirical human functional connectivity in Fig. S1B was derived from preprocessed  
493 functional MRI (fMRI) data of 100 unrelated healthy young adults from HCP (same participants  
494 used to calculate the HCP group-averaged connectome above) [26]. For each participant,  
495 functional connectivity (*FC*) was calculated by taking pairwise Pearson correlations of the BOLD-  
496 fMRI signal across 114 regions (Table S1). A group-averaged functional connectivity was  
497 obtained by taking the average of the individual functional connectivity matrices.

498 *Macaque*. The empirical macaque functional connectivity in Fig. S1B was derived from  
499 preprocessed fMRI data of 8 adult rhesus macaques (same subjects used to calculate the macaque  
500 group-averaged connectome above) [29]. For each subject, *FC* was calculated by taking pairwise  
501 Pearson correlations of the BOLD-fMRI signal across 82 regions [66]. A group-averaged  
502 functional connectivity was obtained by taking the average of the individual functional  
503 connectivity matrices.

#### 504 **Cortical T1w:T2w data**

505 Human and chimpanzee cortical T1w:T2w data, serving as a proxy for myelination, were obtained  
506 from [38]. The T1w:T2w maps were parcellated using our 114-region atlas (Table S1).

#### 507 **Cortical expansion data**

508 Human and chimpanzee cortical expansion data were obtained from [27]. The data represent the  
509 ratio of the normalized cortical surface area of each region in the 114-region atlas (Table S1)  
510 between humans and chimpanzees. The normalization was obtained by dividing each region's  
511 surface area by the whole cortex's total surface area. Hence, an expansion value greater than 1  
512 means that the relevant region in humans is more expanded compared to the same region in  
513 chimpanzees.

#### 514 **Cortical surfaces**

515 For visualization purposes, we mapped some results into template human and chimpanzee inflated  
516 cortical surfaces (Figs. 1A, 1B, 3C, 7A, S10B, S11, and S16) obtained from  
517 <https://balsa.wustl.edu/study/Klr0B>, which is a public repository of data from [38].

#### 518 **Graph theoretical analysis**

519 To investigate the structural property of the connectomes, we leveraged concepts from the field of  
520 graph theory [11,13,74,75]. In particular, we quantified small-world propensity, modularity,  
521 regional clustering coefficient, and regional path length. Small-world propensity quantifies the  
522 extent to which the network exhibits a small-world structure [11]. Modularity quantifies the extent  
523 to which the network may be subdivided into distinct modules (i.e., groups of regions). The  
524 clustering coefficient quantifies the probability of finding a connection between the neighbors of  
525 a given node (region). Specifically, this metric was estimated by calculating the fraction of  
526 triangles around a region. The path length quantifies the level of integration in the network (short  
527 path length implying high integration). Path length corresponds to the total topological distance of

528 the shortest path between two regions. For our weighted connectomes, we defined the topological  
 529 distance to be inversely proportional to the weight of connection (i.e., distance = 1/weight). For  
 530 each brain region, the regional path length was calculated by taking the average of the path lengths  
 531 between that region and all other regions.

### 532 Computational models

533 *Reduced Wong-Wang neural model.* To simulate local neural dynamics on the connectome, we  
 534 used the reduced Wong-Wang biophysical model, also known as the dynamic mean field model,  
 535 which is an established model derived from a mean-field spiking neuronal network [14–17]. Each  
 536 brain region  $i$  is governed by the following nonlinear stochastic differential equation:

$$537 \quad \dot{S}_i = -\frac{S_i}{\tau_s} + \gamma_s(1 - S_i)H(x_i) + D\nu_i(t), \quad (1)$$

$$538 \quad H(x_i) = \frac{ax_i - b}{1 - \exp[-d(ax_i - b)]}, \quad (2)$$

$$539 \quad x_i = wJS_i + GJ \sum_j A_{ij}S_j + I_0, \quad (3)$$

540 where  $S_i$ ,  $H(x_i)$ , and  $x_i$  represent the synaptic response variable, firing rate, and total input current,  
 541 respectively. In the original formulation of the model, the synaptic response variable  $S_i$  in Eq. (1)  
 542 acts as a gating variable that represents the fraction of open (or activated) NMDA channels [14–  
 543 16]. Thus, higher values of  $S_i$  correspond to higher neural activity. The synaptic response variable  
 544 is governed by the time constant  $\tau_s = 0.1$  s, saturation rate  $\gamma_s = 0.641$ , firing rate  $H$ , and independent  
 545 zero-mean Gaussian noise  $\nu_i$  with standard deviation  $D = 0.003$ . The firing rate  $H$  is a nonlinear  
 546 input-output function defined in Eq. (2) governed by the total input current  $x_i$  with constants  $a =$   
 547  $270$  (V nC) $^{-1}$ ,  $b = 109$  Hz, and  $d = 0.154$  s. The total input current  $x_i$  is determined in Eq. (3) by  
 548 the recurrent connection strength  $w$ , synaptic coupling  $J = 0.2609$  nA, global scaling constant  $G =$   
 549  $0.2$ , connection strength  $A_{ij}$  between regions  $i$  and  $j$ , and excitatory subcortical input  $I_0 = 0.33$  nA.  
 550 The parameter values were taken from previous works [16,17]. Note that the value of the global  
 551 scaling constant was fixed for all species. This is to ensure that we can directly compare variations  
 552 in neural dynamics. We simulated the model by numerically solving Eq. (1) using the Euler–  
 553 Maruyama scheme for a time period of 720 s and a time step of 0.01 s. We then calculated the  
 554 time-average value of the synaptic response variable  $\bar{S}$  after removing transients, which we used  
 555 to represent neural dynamics in our analyses.

556 *Balloon-Windkessel hemodynamic model.* To obtain the simulated functional connectivity in Figs.  
 557 2D and S1, we fed the neural activity  $S_i$  from Eq. (1) to the Balloon-Windkessel hemodynamic  
 558 model, which is a well-established model for simulating BOLD-fMRI signals [76]. Note though  
 559 that this is a simple approximation to more detailed hemodynamic models [77]. Each brain region  
 560  $i$  is governed by the following nonlinear differential equations:

$$561 \quad \dot{z}_i = S_i - \kappa z_i - \gamma(f_i - 1), \quad (4)$$

$$562 \quad \dot{f}_i = z_i, \quad (5)$$

$$563 \quad \dot{v}_i = \frac{1}{\tau}(f_i - v_i^{1/\alpha}), \quad (6)$$

$$564 \quad \dot{q}_i = \frac{1}{\tau} \left\{ \frac{f_i}{\rho} [1 - (1 - \rho)^{1/f_i}] - q_i v_i^{\frac{1}{\alpha}-1} \right\}, \quad (7)$$

565 
$$\dot{Y}_i = V_0 \left[ k_1(1 - q_i) + k_2 \left( 1 - \frac{q_i}{v_i} \right) + k_3(1 - v_i) \right], \quad (8)$$

566 where  $z_i$ ,  $f_i$ ,  $v_i$ ,  $q_i$ , and  $Y_i$  represent the vasodilatory signal, blood inflow, blood volume,  
 567 deoxyhemoglobin content, and BOLD-fMRI signal, respectively. The model parameters and their  
 568 values are defined as follows: signal decay rate  $\kappa = 0.65 \text{ s}^{-1}$ , elimination rate  $\gamma = 0.41 \text{ s}^{-1}$ ,  
 569 hemodynamic transit time  $\tau = 0.98 \text{ s}$ , Grubb's exponent  $\alpha = 0.32$ , resting oxygen extraction  
 570 fraction  $\rho = 0.34$ , resting blood volume fraction  $V_0 = 0.02$ , and fMRI parameters  $k_1 = 4.10$ ,  $k_2 =$   
 571  $0.58$ ,  $k_3 = 0.53$ . The parameter values were taken from previous works [76]. We simulated the  
 572 model for a time period of 720 s and the time series were downsampled to a temporal resolution  
 573 of 0.72 s to match the resolution of typical empirical BOLD-fMRI signals. Functional connectivity  
 574 ( $FC$ ) was calculated by taking pairwise Pearson correlations of  $Y_i$  (after removing transients) across  
 575 all regions. The within-network functional connectivity in Fig. 3D was obtained by taking the  
 576 average of the  $FC$  between regions comprising each network.

577 *Wilson-Cowan neural model.* To show that our results generalize beyond our choice of biophysical  
 578 model, we also simulated local neural dynamics using the Wilson-Cowan model [78] (Fig. S9).  
 579 We chose this model because of its known ability to reproduce diverse large-scale neural  
 580 phenomena [79]. Each brain region  $i$  comprises interacting populations of excitatory ( $E$ ) and  
 581 inhibitory ( $I$ ) neurons governed by the following nonlinear stochastic differential equations:

582 
$$\dot{S}_i^E = \frac{1}{\tau_E} [-S_i^E + (1 - S_i^E)H_E(x_i^E) + D_E\nu_i^E(t)], \quad (9)$$

584 
$$\dot{S}_i^I = \frac{1}{\tau_I} [-S_i^I + (1 - S_i^I)H_I(x_i^I) + D_I\nu_i^I(t)], \quad (10)$$

585 
$$H_E(x_i^E) = \frac{1}{1 + \exp[-a_E(x_i^E - \mu_E)]}, \quad (11)$$

586 
$$H_I(x_i^I) = \frac{1}{1 + \exp[-a_I(x_i^I - \mu_I)]}, \quad (12)$$

588 
$$x_i^E = w_{EE}S_i^E - w_{EI}S_i^I + G \sum_j A_{ij}S_j^E + G_E P_E, \quad (13)$$

589 
$$x_i^I = w_{IE}S_i^E - w_{II}S_i^I, \quad (14)$$

591 where  $S_i$ ,  $H(x_i)$ , and  $x_i$  represent the firing rate, non-linear activation function, and weighted sum  
 592 of firing rates, respectively, for  $E$  and  $I$  populations. The dynamics of the firing rates  $S_i^E$  and  $S_i^I$  in  
 593 Eqs. (9) and (10) are parameterized by the excitatory time constant  $\tau_E = 2.5 \times 10^{-3} \text{ s}$ , inhibitory time  
 594 constant  $\tau_I = 3.75 \times 10^{-3} \text{ s}$ , activation functions  $H_E$  and  $H_I$ , and independent zero-mean Gaussian  
 595 noise  $\nu_i^E$  and  $\nu_i^I$  with standard deviations  $D_E = 5 \times 10^{-5}$  and  $D_I = 5 \times 10^{-5}$ , respectively. The activation  
 596 functions  $H_E$  and  $H_I$  in Eqs. (11) and (12) are defined by sigmoids parameterized by the gain  
 597 constants  $a_E = 1.5$  and  $a_I = 1.5$  and firing thresholds  $\mu_E = 3$  and  $\mu_I = 3$ .  $x_i^E$  and  $x_i^I$  are determined  
 598 in Eqs. (13) and (14) by the excitatory-excitatory recurrent connection strength  $w_{EE} = 16$ ,  
 599 excitatory-inhibitory connection strength  $w_{EI} = 12$ , inhibitory-excitatory connection strength  $w_{IE} = 15$ ,  
 600 inhibitory-inhibitory recurrent connection strength  $w_{II} = 3$ , global scaling constant  $G = 2$ ,  
 601 connection strength  $A_{ij}$  between regions  $i$  and  $j$ , and excitatory drive  $P_E = 1$  scaled by  $G_E = 0.5$ .

602 The parameter values were taken from previous works [78,79]. We simulated the model by  
 603 numerically solving Eqs. (9) and (10) using the Euler-Maruyama scheme for a time period of 15 s  
 604 and a time step of 0.001 s. We then calculated the time-average value of the excitatory firing rate  
 605  $S^E$  after removing transients, which we used to represent neural dynamics in our analyses.

606 *Drift-diffusion model.* To simulate the ability of human and chimpanzee connectomes to reach a  
 607 binary decision, we implemented a computational drift-diffusion model [35–37] (Fig. 6B). Each  
 608 brain region  $i$  is governed by the following stochastic differential equation:

$$609 \quad \dot{y}_i = \beta_i + \lambda y_i - \sum_j L_{ij} y_j + D \nu_i(t), \quad (15)$$

610 where  $y_i$  is the evidence at time  $t$ ,  $\beta_i$  is the drift rate,  $\lambda$  is the self-coupling parameter,  $L_{ij}$  is the  
 611 Laplacian weight of the connection between regions  $i$  and  $j$ , and  $\nu_i$  is an independent zero-mean  
 612 Gaussian noise with standard deviation  $D$ . The Laplacian matrix  $L$  is obtained via  $L = \mathfrak{D} - A$ ,  
 613 where  $A$  is the connectivity matrix and  $\mathfrak{D}$  is a diagonal matrix of node strengths such that the  $i$ th  
 614 diagonal element is  $\sum_j A_{ij}$ . To focus on the contribution of the connectome itself, we fixed the  
 615 drift rates of the regions to  $\beta_i = 1$  and  $D = 1$ . We verified that changing these parameter values  
 616 did not change the results of the study. We also set  $\lambda = 0$  in our main results in Fig. 6, but also  
 617 extensively varied it in Fig. S15 to investigate the effects of excitation (i.e.,  $\lambda > 0$ ) and inhibition  
 618 (i.e.,  $\lambda < 0$ ) on the decision-making capacity of the connectomes. Through the simple diffusion  
 619 process implemented by the model, each region accumulates the decision evidence through time  
 620 until it reaches a boundary threshold  $\theta = \pm 1$  where a decision is said to be reached. Without loss  
 621 of generality, we assumed  $\theta = 1$  to be the correct decision (Fig. 6C). We simulated the model by  
 622 numerically solving Eq. (15) using the Euler-Maruyama scheme for a time period of 5 s and a time  
 623 step of 0.01 s. We then calculated the decision accuracy versus time of each region across an  
 624 ensemble of 1000 trials (Fig. 6D).

## 625 Measures of neural dynamics properties

626 *Neural dynamic range.* For each brain region, we analyzed its response function reflecting how  
 627 mean activity changes versus global modulations in the strength of recurrent connections (i.e.,  $\bar{S}$   
 628 versus  $w$  for the reduced Wong-Wang model and  $S^E$  versus  $w_{EE}$  for the Wilson-Cowan model).  
 629 The response function was characterized in terms of the neural dynamic range, mathematically  
 630 defined as:

$$631 \quad \text{dynamic range} = 10 \log_{10} \frac{w_{90}}{w_{10}}, \quad (16)$$

632 where  $w_x$  is the corresponding global recurrent strength at  $\bar{S}_x$ , with  $x = \{10, 90\}$  and

$$633 \quad \bar{S}_x = \bar{S}_{\min} + \left( \frac{x}{100} \right) (\bar{S}_{\max} - \bar{S}_{\min}). \quad (17)$$

634 We then pooled together the dynamic ranges of brain regions for each species of interest to create  
 635 a distribution with standard deviation  $\sigma$ .

636 *Neural timescale.* To estimate neural timescales for each brain region, we simulated neural activity  
 637 via the model described in Eqs. (1) to (3). We used a global recurrent strength of  $w = 0.45$  to  
 638 produce neural dynamics in a biologically plausible regime; i.e., dynamics with relatively low  
 639 firing rate and not fully synchronized [80]. Following recent studies [31,32], we quantified the  
 640 neural timescale of each brain region  $i$  by fitting the autocorrelation of  $S_i(t)$  with a single  
 641 exponential decay function (via non-linear least-squares) with form

642                           $\text{autocorrelation}_i = c_1 e^{-\frac{t}{\tau_i}} + c_2,$                           (18)

643 where  $c_1$  and  $c_2$  are fitting constants and  $\tau_i$  is the estimated neural timescale (Fig. S13). We verified  
644 that fitting with a double exponential decay function did not change the results of the study.

645 **Additional confirmatory analyses**

646 We performed several confirmatory analyses to check the robustness of our results. In particular,  
647 we addressed potential effects of differences in individual-specific connectomes (Fig. S2),  
648 differences in connection density (Fig. S3), variability of connection strengths across participants  
649 (Fig. S4), differences in human and chimpanzee data sample size (Fig. S5), and existence of  
650 activity propagation delays between brain regions (Fig. S6). The procedures for each confirmatory  
651 analysis are described below.

652 *Individual-specific analysis.* Brain dynamics resulting from group-averaged connectomes could  
653 differ when individual-specific connectomes are used. Hence, we repeated the analysis in Fig. 3 to  
654 the connectome of each human and chimpanzee participant to produce Fig. S2.

655 *Connection density.* The resulting connection densities of the group-averaged human and  
656 chimpanzee connectomes were different (13.7% versus 11.6%, respectively). Hence, we created a  
657 new human connectome by pruning weak connections such that its density matches the density of  
658 the chimpanzee connectome. We then repeated the analysis in Fig. 3 to produce Fig. S3.

659 *Inter-individual variability of connection strengths.* The quality of connectomic data across  
660 participants in each species may be different due to potential additional confounds unable to be  
661 corrected by the implemented data preprocessing methods. Thus, within each species, we  
662 calculated the variability of weights of each connection  $A_{ij}$  across participants ( $\sigma_{ij}^{\text{human}}$  and  
663  $\sigma_{ij}^{\text{chimpanzee}}$ ). We then rescaled the human and chimpanzee connectomes to match each other's  
664 inter-individual variability. Specifically, we multiplied the human connectome weights by  
665  $\sigma_{ij}^{\text{chimpanzee}}/\sigma_{ij}^{\text{human}}$  and the chimpanzee connectome weights by  $\sigma_{ij}^{\text{human}}/\sigma_{ij}^{\text{chimpanzee}}$ . We then  
666 repeated the analysis in Fig. 3 to produce Fig. S4.

667 *Sample sizes.* The sample sizes of the human and chimpanzee connectomic data differ ( $N = 58$  for  
668 humans and  $N = 22$  for chimpanzees). Hence, we randomly sampled 22 human participants to  
669 match the sample size of the chimpanzee data and calculated the corresponding new group-  
670 averaged human connectome. The resampling procedure was repeated for 100 trials. For each trial,  
671 we repeated the analysis in Fig. 3 to produce Fig. S5.

672 *Activity propagation delay.* The model we used, as described in Eqs. (1) to (3), assumes that the  
673 activity of a brain region propagates and affects instantaneously the activity of all other regions  
674 connected to it (i.e., propagation time delay is zero). However, due to the spatial embedding of the  
675 brain and the finiteness of activity propagation speeds, we modified the second term of Eq. (3) to  
676 incorporate non-zero time delays as follows:

677                           $x_i(t) = wJS_i(t) + GJ \sum_j A_{ij}S_j(t - t_{ij}^d) + I_0,$                           (19)

678 where  $t_{ij}^d$  is the propagation time delay between regions  $i$  and  $j$ . We approximated the time delays  
679 as  $t_{ij}^d = D_{ij}/v$ , where  $D_{ij}$  is the Euclidean distance between the centroids of regions  $i$  and  $j$  and  $v$   
680 is the propagation speed. We assumed  $v$  to be a constant with value 10 m/s [81] and was the same

for both human and chimpanzee brains; choosing other values of  $\nu$  did not change our results. Meanwhile,  $D_{ij}$  is specific to human and chimpanzee brains to account for differences in brain sizes. In our analysis, we obtained  $D_{ij}$  from one randomly chosen representative human and chimpanzee; the resulting distributions of time delays are shown in Fig. S6A. We then repeated the analysis in Fig. 3 to produce Figs. S6B and S6C.

*Heterogeneous excitatory input.* The model we used, as described in Eqs. (1) to (3), assumes that the activities of brain regions are driven by a constant excitatory input  $I_0$ . We tested whether varying  $I_0$  per region affects the results of the study. In particular, we incorporated a gradient of excitatory input across the anatomical cortical hierarchy, with unimodal regions having higher input and transmodal regions having lower input [17]. Inspired by previous works using a region's total connection strength as a proxy of the cortical hierarchy [82,83], we modified the last term of Eq. (3) as follows:

$$x_i = wJS_i + GJ \sum_j A_{ij}S_j + I_i, \quad (20)$$

$$I_i = I_{\max} - (I_{\max} - I_{\min}) \left( \frac{\text{rank}(s_i) - 1}{N - 1} \right), \quad (21)$$

where  $I_{\max} = 0.33$  nA,  $I_{\min} = 0.28$  nA,  $s_i = \sum_j A_{ij}$  is the total connection strength of region  $i$ , and  $N$  is the total number of regions. The resulting excitatory input of regions in human and chimpanzee brains are shown in Fig. S7A. We then repeated the analysis in Fig. 3 to produce Figs. S7B and S7C. Note that the values of  $I_{\max}$  and  $I_{\min}$  were chosen to match the spread of estimated excitatory inputs found in [17]. However, we verified that using other values of  $I_{\max}$  and  $I_{\min}$  did not change the results of the study.

## DATA AND CODE AVAILABILITY

All source data and MATLAB codes to perform sample simulations, analyze results, and generate the main and supplementary figures of this study are openly available at <https://github.com/jchrispang/evolution-brain-tuning>.

## REFERENCES

1. Seyfarth, R.M., and Cheney, D.L. (2014). The evolution of language from social cognition. *Current Opinion in Neurobiology* *28*, 5–9. 10.1016/j.conb.2014.04.003.
2. Rilling, J.K. (2006). Human and NonHuman primate brains: Are they allometrically scaled versions of the same design? *Evolutionary Anthropology* *15*, 65–77. 10.1002/evan.20095.
3. Rilling, J.K. (2014). Comparative primate neuroimaging: Insights into human brain evolution. *Trends in Cognitive Sciences* *18*, 46–55. 10.1016/j.tics.2013.09.013.
4. Smaers, J.B., Gómez-Robles, A., Parks, A.N., and Sherwood, C.C. (2017). Exceptional Evolutionary Expansion of Prefrontal Cortex in Great Apes and Humans. *Current Biology* *27*, 714–720. 10.1016/j.cub.2017.05.015.
5. Avants, B.B., Schoenemann, P.T., and Gee, J.C. (2006). Lagrangian frame diffeomorphic image registration: Morphometric comparison of human and chimpanzee cortex. *Medical Image Analysis* *10*, 397–412. 10.1016/j.media.2005.03.005.

- 722 6. Van Essen, D.C., and Dierker, D.L. (2007). Surface-based and probabilistic atlases of  
723 primate cerebral cortex. *Neuron* *56*, 209–225. 10.1016/j.neuron.2007.10.015.
- 724 7. Ardesch, D.J., Scholtens, L.H., Li, L., Preuss, T.M., Rilling, J.K., and van den Heuvel, M.P.  
725 (2019). Evolutionary expansion of connectivity between multimodal association areas in the  
726 human brain compared with chimpanzees. *Proceedings of the National Academy of Sciences  
727 of the United States of America* *116*, 7101–7106. 10.1073/pnas.1818512116.
- 728 8. van den Heuvel, M.P., Bullmore, E.T., and Sporns, O. (2016). Comparative Connectomics.  
729 Trends in Cognitive Sciences *20*, 345–361. 10.1016/j.tics.2016.03.001.
- 730 9. Breakspear, M. (2017). Dynamic models of large-scale brain activity. *Nature Neuroscience*  
731 *20*, 340–352. 10.1038/nn.4497.
- 732 10. Van Den Heuvel, M.P., Scholtens, L.H., De Lange, S.C., Pijnenburg, R., Cahn, W., Van  
733 Haren, N.E.M., Sommer, I.E., Bozzali, M., Koch, K., Boks, M.P., *et al.* (2019). Evolutionary  
734 modifications in human brain connectivity associated with schizophrenia. *Brain* *142*, 3991–  
735 4002. 10.1093/brain/awz330.
- 736 11. Muldoon, S.F., Bridgeford, E.W., and Bassett, D.S. (2016). Small-world propensity and  
737 weighted brain networks. *Scientific Reports* *6*, 22057. 10.1038/srep22057.
- 738 12. Bullmore, E., and Sporns, O. (2009). Complex brain networks: Graph theoretical analysis of  
739 structural and functional systems. *Nature Reviews Neuroscience* *10*, 186–198.  
740 10.1038/nrn2575.
- 741 13. Rubinov, M., and Sporns, O. (2010). Complex network measures of brain connectivity: Uses  
742 and interpretations. *NeuroImage* *52*, 1059–1069. 10.1016/j.neuroimage.2009.10.003.
- 743 14. Wang, X.J. (2002). Probabilistic decision making by slow reverberation in cortical circuits.  
744 *Neuron* *36*, 955–968. 10.1016/S0896-6273(02)01092-9.
- 745 15. Wong, K.F., and Wang, X.J. (2006). A recurrent network mechanism of time integration in  
746 perceptual decisions. *Journal of Neuroscience* *26*, 1314–1328. 10.1523/JNEUROSCI.3733-  
747 05.2006.
- 748 16. Deco, G., Ponce-Alvarez, A., Mantini, D., Romani, G.L., Hagmann, P., and Corbetta, M.  
749 (2013). Resting-state functional connectivity emerges from structurally and dynamically  
750 shaped slow linear fluctuations. *Journal of Neuroscience* *33*, 11239–11252.  
751 10.1523/JNEUROSCI.1091-13.2013.
- 752 17. Wang, P., Kong, R., Kong, X., Liégeois, R., Orban, C., Deco, G., Van Den Heuvel, M.P.,  
753 and Yeo, B.T.T. (2019). Inversion of a large-scale circuit model reveals a cortical hierarchy  
754 in the dynamic resting human brain. *Science Advances* *5*, eaat7854. 10.1126/sciadv.aat7854.
- 755 18. Shine, J.M., Bissett, P.G., Bell, P.T., Koyejo, O., Balsters, J.H., Gorgolewski, K.J., Moodie,  
756 C.A., and Poldrack, R.A. (2016). The Dynamics of Functional Brain Networks: Integrated  
757 Network States during Cognitive Task Performance. *Neuron* *92*, 544–554.  
758 10.1016/j.neuron.2016.09.018.
- 759 19. Shine, J.M. (2019). Neuromodulatory Influences on Integration and Segregation in the Brain.  
760 Trends in Cognitive Sciences *23*, 572–583. 10.1016/j.tics.2019.04.002.
- 761 20. Wainstein, G., Müller, E.J., Taylor, N., Munn, B., and Shine, J.M. (2022). The role of the  
762 locus coeruleus in shaping adaptive cortical melodies. *Trends in Cognitive Sciences*.  
763 10.1016/j.tics.2022.03.006.
- 764 21. Shine, J.M., Müller, E.J., Munn, B., Cabral, J., Moran, R.J., and Breakspear, M. (2021).  
765 Computational models link cellular mechanisms of neuromodulation to large-scale neural  
766 dynamics. *Nature Neuroscience* *24*, 765–776. 10.1038/s41593-021-00824-6.

- 767 22. Leenders, A.G.M., and Sheng, Z.H. (2005). Modulation of neurotransmitter release by the  
768 second messenger-activated protein kinases: Implications for presynaptic plasticity.  
769 *Pharmacology and Therapeutics* *105*, 69–84. 10.1016/j.pharmthera.2004.10.012.
- 770 23. Bang, D., Kishida, K.T., Lohrenz, T., White, J.P., Laxton, A.W., Tatter, S.B., Fleming, S.M.,  
771 and Montague, P.R. (2020). Sub-second Dopamine and Serotonin Signaling in Human  
772 Striatum during Perceptual Decision-Making. *Neuron* *108*, 999-1010.e6.  
773 10.1016/j.neuron.2020.09.015.
- 774 24. Kinouchi, O., and Copelli, M. (2006). Optimal dynamical range of excitable networks at  
775 criticality. *Nature Physics* *2*, 348–351. 10.1038/nphys289.
- 776 25. Shafiei, G., Markello, R.D., De Wael, R.V., Bernhardt, B.C., Fulcher, B.D., and Misic, B.  
777 (2020). Topographic gradients of intrinsic dynamics across neocortex. *eLife* *9*, 1–24.  
778 10.7554/eLife.62116.
- 779 26. Van Essen, D.C., Smith, S.M., Barch, D.M., Behrens, T.E.J., Yacoub, E., and Ugurbil, K.  
780 (2013). The WU-Minn Human Connectome Project: An overview. *NeuroImage* *80*, 62–79.  
781 10.1016/j.neuroimage.2013.05.041.
- 782 27. Wei, Y., de Lange, S.C., Scholtens, L.H., Watanabe, K., Ardesch, D.J., Jansen, P.R., Savage,  
783 J.E., Li, L., Preuss, T.M., Rilling, J.K., *et al.* (2019). Genetic mapping and evolutionary  
784 analysis of human-expanded cognitive networks. *Nature Communications* *10*, 4839.  
785 10.1038/s41467-019-12764-8.
- 786 28. Thomas Yeo, B.T., Krienen, F.M., Sepulcre, J., Sabuncu, M.R., Lashkari, D., Hollinshead,  
787 M., Roffman, J.L., Smoller, J.W., Zöllei, L., Polimeni, J.R., *et al.* (2011). The organization  
788 of the human cerebral cortex estimated by intrinsic functional connectivity. *Journal of  
789 Neurophysiology* *106*, 1125–1165. 10.1152/jn.00338.2011.
- 790 29. Shen, K., Bezgin, G., Schirner, M., Ritter, P., Everling, S., and McIntosh, A.R. (2019). A  
791 macaque connectome for large-scale network simulations in TheVirtualBrain. *Scientific Data*  
792 *6*, 123. 10.1038/s41597-019-0129-z.
- 793 30. Majka, P., Bai, S., Bakola, S., Bednarek, S., Chan, J.M., Jermakow, N., Passarelli, L., Reser,  
794 D.H., Theodoni, P., Worthy, K.H., *et al.* (2020). Open access resource for cellular-resolution  
795 analyses of corticocortical connectivity in the marmoset monkey. *Nature Communications*  
796 *11*, 1133. 10.1038/s41467-020-14858-0.
- 797 31. Murray, J.D., Bernacchia, A., Freedman, D.J., Romo, R., Wallis, J.D., Cai, X., Padoa-  
798 Schioppa, C., Pasternak, T., Seo, H., Lee, D., *et al.* (2014). A hierarchy of intrinsic  
799 timescales across primate cortex. *Nature Neuroscience* *17*, 1661–1663. 10.1038/nn.3862.
- 800 32. Gao, R., Van den Brink, R.L., Pfeffer, T., and Voytek, B. (2020). Neuronal timescales are  
801 functionally dynamic and shaped by cortical microarchitecture. *eLife* *9*, e61277.  
802 10.7554/eLife.61277.
- 803 33. Kiebel, S.J., Daunizeau, J., and Friston, K.J. (2008). A hierarchy of time-scales and the brain.  
804 *PLoS Computational Biology* *4*, e1000209. 10.1371/journal.pcbi.1000209.
- 805 34. Cocchi, L., Yang, Z., Zalesky, A., Stelzer, J., Hearne, L.J., Gollo, L.L., and Mattingley, J.B.  
806 (2017). Neural decoding of visual stimuli varies with fluctuations in global network  
807 efficiency. *Human Brain Mapping* *38*, 3069–3080. 10.1002/hbm.23574.
- 808 35. Ratcliff, R., Smith, P.L., Brown, S.D., and McKoon, G. (2016). Diffusion Decision Model:  
809 Current Issues and History. *Trends in Cognitive Sciences* *20*, 260–281.  
810 10.1016/j.tics.2016.01.007.

- 811 36. Carland, M.A., Thura, D., and Cisek, P. (2015). The urgency-gating model can explain the  
812 effects of early evidence. *Psychonomic Bulletin and Review* 22, 1830–1838.  
813 10.3758/s13423-015-0851-2.
- 814 37. Lam, N.H., Borduqui, T., Hallak, J., Roque, A., Anticevic, A., Krystal, J.H., Wang, X.J., and  
815 Murray, J.D. (2022). Effects of Altered Excitation-Inhibition Balance on Decision Making in  
816 a Cortical Circuit Model. *Journal of Neuroscience* 42, 1035–1053.  
817 10.1523/JNEUROSCI.1371-20.2021.
- 818 38. Hayashi, T., Hou, Y., Glasser, M.F., Autio, J.A., Knoblauch, K., Inoue-Murayama, M.,  
819 Coalson, T., Yacoub, E., Smith, S., Kennedy, H., *et al.* (2021). The nonhuman primate  
820 neuroimaging and neuroanatomy project. *NeuroImage* 229, 117726.  
821 10.1016/j.neuroimage.2021.117726.
- 822 39. Glasser, M.F., Goyal, M.S., Preuss, T.M., Raichle, M.E., and Van Essen, D.C. (2014).  
823 Trends and properties of human cerebral cortex: Correlations with cortical myelin content.  
824 *NeuroImage* 93, 165–175. 10.1016/j.neuroimage.2013.03.060.
- 825 40. Burt, J.B., Demirtaş, M., Eckner, W.J., Navejar, N.M., Ji, J.L., Martin, W.J., Bernacchia, A.,  
826 Anticevic, A., and Murray, J.D. (2018). Hierarchy of transcriptomic specialization across  
827 human cortex captured by structural neuroimaging topography. *Nature Neuroscience* 21,  
828 1251–1259. 10.1038/s41593-018-0195-0.
- 829 41. Ponce de León, M.S., Bienvenu, T., Marom, A., Engel, S., Tafforeau, P., Warren, J.L.A.,  
830 Lordkipanidze, D., Kurniawan, I., Murti, D.B., Suriyanto, R.A., *et al.* (2021). The primitive  
831 brain of early Homo. *Science* 372, 165–171. 10.1126/science.aaz0032.
- 832 42. Zhang, D., Yan, X., She, L., Wen, Y., and Poo, M.M. (2020). Global enhancement of cortical  
833 excitability following coactivation of large neuronal populations. *Proceedings of the  
834 National Academy of Sciences of the United States of America* 117, 20254–20264.  
835 10.1073/PNAS.1914869117.
- 836 43. Gollo, L.L., Copelli, M., and Roberts, J.A. (2016). Diversity improves performance in  
837 excitable networks. *PeerJ* 4, e1912. 10.7717/peerj.1912.
- 838 44. Gollo, L.L., Roberts, J.A., Cropley, V.L., Di Biase, M.A., Pantelis, C., Zalesky, A., and  
839 Breakspear, M. (2018). Fragility and volatility of structural hubs in the human connectome.  
840 *Nature Neuroscience* 21, 1107–1116. 10.1038/s41593-018-0188-z.
- 841 45. Felleman, D.J., and Van Essen, D.C. (1991). Distributed hierarchical processing in the  
842 primate cerebral cortex. *Cerebral Cortex* 1, 1–47.
- 843 46. Mesulam, M.M. (1998). From sensation to cognition. *Brain* 121, 1013–1052.  
844 10.1093/brain/121.6.1013.
- 845 47. Wagstyl, K., Ronan, L., Goodyer, I.M., and Fletcher, P.C. (2015). Cortical thickness  
846 gradients in structural hierarchies. *NeuroImage* 111, 241–250.  
847 10.1016/j.neuroimage.2015.02.036.
- 848 48. Margulies, D.S., Ghosh, S.S., Goulas, A., Falkiewicz, M., Huntenburg, J.M., Langs, G.,  
849 Bezgin, G., Eickhoff, S.B., Castellanos, F.X., Petrides, M., *et al.* (2016). Situating the  
850 default-mode network along a principal gradient of macroscale cortical organization.  
851 *Proceedings of the National Academy of Sciences of the United States of America* 113,  
852 12574–12579. 10.1073/pnas.1608282113.
- 853 49. Hasson, U., Yang, E., Vallines, I., Heeger, D.J., and Rubin, N. (2008). A hierarchy of  
854 temporal receptive windows in human cortex. *Journal of Neuroscience* 28, 2539–2550.  
855 10.1523/JNEUROSCI.5487-07.2008.

- 856 50. Charvet, C.J., Cahalane, D.J., and Finlay, B.L. (2015). Systematic, cross-cortex variation in  
857 neuron numbers in rodents and primates. *Cerebral Cortex* 25, 147–160.  
858 10.1093/cercor/bht214.
- 859 51. Collins, C.E., Airey, D.C., Young, N.A., Leitch, D.B., and Kaas, J.H. (2010). Neuron  
860 densities vary across and within cortical areas in primates. *Proceedings of the National  
861 Academy of Sciences of the United States of America* 107, 15927–15932.  
862 10.1073/pnas.1010356107.
- 863 52. Collins, C.E., Turner, E.C., Sawyer, E.K., Reed, J.L., Young, N.A., Flaherty, D.K., and  
864 Kaas, J.H. (2016). Cortical cell and neuron density estimates in one chimpanzee hemisphere.  
865 *Proceedings of the National Academy of Sciences of the United States of America* 113, 740–  
866 745. 10.1073/pnas.1524208113.
- 867 53. Martin, C.F., Bhui, R., Bossaerts, P., Matsuzawa, T., and Camerer, C. (2014). Chimpanzee  
868 choice rates in competitive games match equilibrium game theory predictions. *Scientific  
869 Reports* 4, 5182. 10.1038/srep05182.
- 870 54. Tomasello, M., Carpenter, M., Call, J., Behne, T., and Moll, H. (2005). Understanding and  
871 sharing intentions: The origins of cultural cognition. *Behavioral and Brain Sciences* 28, 675–  
872 691. 10.1017/S0140525X05000129.
- 873 55. Thornton, A., Clayton, N.S., and Grodzinski, U. (2012). Animal minds: From computation to  
874 evolution. *Philosophical Transactions of the Royal Society B: Biological Sciences* 367,  
875 2670–2676. 10.1098/rstb.2012.0270.
- 876 56. Herrmann, E., Call, J., Hernández-Lloreda, M.V., Hare, B., and Tomasello, M. (2007).  
877 Humans have evolved specialized skills of social cognition: The cultural intelligence  
878 hypothesis. *Science* 317, 1360–1366. 10.1126/science.1146282.
- 879 57. Buckner, R.L., Andrews-Hanna, J.R., and Schacter, D.L. (2008). The brain's default  
880 network: Anatomy, function, and relevance to disease. *Annals of the New York Academy of  
881 Sciences* 1124, 1–38. 10.1196/annals.1440.011.
- 882 58. Spreng, R.N., Mar, R.A., and Kim, A.S.N. (2009). The common neural basis of  
883 autobiographical memory, prospection, navigation, theory of mind, and the default mode: A  
884 quantitative meta-analysis. *Journal of Cognitive Neuroscience* 21, 489–510.  
885 10.1162/jocn.2008.21029.
- 886 59. Bruner, E., Preuss, T.M., Chen, X., and Rilling, J.K. (2017). Evidence for expansion of the  
887 precuneus in human evolution. *Brain Structure and Function* 222, 1053–1060.  
888 10.1007/s00429-015-1172-y.
- 889 60. Xu, T., Nenning, K.H., Schwartz, E., Hong, S.J., Vogelstein, J.T., Goulas, A., Fair, D.A.,  
890 Schroeder, C.E., Margulies, D.S., Smallwood, J., et al. (2020). Cross-species functional  
891 alignment reveals evolutionary hierarchy within the connectome. *NeuroImage* 223, 117346.  
892 10.1016/j.neuroimage.2020.117346.
- 893 61. Buckner, R.L., and Krienen, F.M. (2013). The evolution of distributed association networks  
894 in the human brain. *Trends in Cognitive Sciences* 17, 648–665. 10.1016/j.tics.2013.09.017.
- 895 62. Burkart, J.M., Schubiger, M.N., and Van Schaik, C.P. (2017). The evolution of general  
896 intelligence. *Behavioral and Brain Sciences* 40, e195. 10.1017/S0140525X16000959.
- 897 63. Assaf, Y., Bouznach, A., Zomet, O., Marom, A., and Yovel, Y. (2020). Conservation of  
898 brain connectivity and wiring across the mammalian class. *Nature Neuroscience* 23, 805–  
899 808. 10.1038/s41593-020-0641-7.
- 900 64. Roxin, A. (2019). Drift–diffusion models for multiple-alternative forced-choice decision  
901 making. *Journal of Mathematical Neuroscience* 9. 10.1186/s13408-019-0073-4.

- 902 65. Desikan, R.S., Ségonne, F., Fischl, B., Quinn, B.T., Dickerson, B.C., Blacker, D., Buckner,  
903 R.L., Dale, A.M., Maguire, R.P., Hyman, B.T., *et al.* (2006). An automated labeling system  
904 for subdividing the human cerebral cortex on MRI scans into gyral based regions of interest.  
905 NeuroImage 31, 968–980. 10.1016/j.neuroimage.2006.01.021.
- 906 66. Kötter, R., and Wanke, E. (2005). Mapping brains without coordinates. Philosophical  
907 Transactions of the Royal Society B: Biological Sciences 360, 751–766.  
908 10.1098/rstb.2005.1625.
- 909 67. Paxinos, G., Watson, C., Petrides, M., Rosa, M.G.P.;, and Tokuno, H. (2012). The Marmoset  
910 Brain in Stereotaxic Coordinates. In (Elsevier Academic Press).
- 911 68. Tournier, J.D., Calamante, F., and Connelly, A. (2012). MRtrix: Diffusion tractography in  
912 crossing fiber regions. International Journal of Imaging Systems and Technology 22, 53–66.  
913 10.1002/ima.22005.
- 914 69. Smith, R.E., Tournier, J.D., Calamante, F., and Connelly, A. (2012). Anatomically-  
915 constrained tractography: Improved diffusion MRI streamlines tractography through  
916 effective use of anatomical information. NeuroImage 62, 1924–1938.  
917 10.1016/j.neuroimage.2012.06.005.
- 918 70. Smith, R.E., Tournier, J.D., Calamante, F., and Connelly, A. (2015). SIFT2: Enabling dense  
919 quantitative assessment of brain white matter connectivity using streamlines tractography.  
920 NeuroImage 119, 338–351. 10.1016/j.neuroimage.2015.06.092.
- 921 71. Schaefer, A., Kong, R., Gordon, E.M., Laumann, T.O., Zuo, X.N., Holmes, A.J., Eickhoff,  
922 S.B., and Yeo, B.T.T. (2018). Local-global parcellation of the human cerebral cortex from  
923 intrinsic functional connectivity mri. Cerebral Cortex 28, 3095–3114. 10.1093/cercor/bhx17.
- 924 72. Kötter, R. (2004). Online retrieval, processing, and visualization of primate connectivity data  
925 from the CoCoMac database. Neuroinformatics 2, 127–144. 10.1385/NI:2:2:127.
- 926 73. Honey, C.J., Kötter, R., Breakspear, M., and Sporns, O. (2007). Network structure of  
927 cerebral cortex shapes functional connectivity on multiple time scales. Proceedings of the  
928 National Academy of Sciences of the United States of America 104, 10240–10245.  
929 10.1073/pnas.0701519104.
- 930 74. Bullmore, E., and Sporns, O. (2009). Complex brain networks: Graph theoretical analysis of  
931 structural and functional systems. Nature Reviews Neuroscience 10, 186–198.  
932 10.1038/nrn2575.
- 933 75. Fornito, A., Zalesky, A., and Bullmore, E.T. (2016). Fundamentals of Brain Network  
934 Analysis 10.1016/C2012-0-06036-X.
- 935 76. Stephan, K.E., Weiskopf, N., Drysdale, P.M., Robinson, P.A., and Friston, K.J. (2007).  
936 Comparing hemodynamic models with DCM. NeuroImage 38, 387–401.  
937 10.1016/j.neuroimage.2007.07.040.
- 938 77. Pang, J.C., Robinson, P.A., Aquino, K.M., and Vasan, N. (2017). Effects of astrocytic  
939 dynamics on spatiotemporal hemodynamics: Modeling and enhanced data analysis.  
940 NeuroImage 147, 994–1005. 10.1016/j.neuroimage.2016.10.023.
- 941 78. Wilson, H.R., and Cowan, J.D. (1972). Excitatory and Inhibitory Interactions in Localized  
942 Populations of Model Neurons. Biophysical Journal 12, 1–24. 10.1016/S0006-  
943 3495(72)86068-5.
- 944 79. Papadopoulos, L., Lynn, C.W., Battaglia, D., and Bassett, D.S. (2020). Relations between  
945 large-scale brain connectivity and effects of regional stimulation depend on collective  
946 dynamical state. PLoS Computational Biology 16, e1008144. 10.1371/journal.pcbi.1008144.

- 947 80. Cocchi, L., Gollo, L.L., Zalesky, A., and Breakspear, M. (2017). Criticality in the brain: A  
948 synthesis of neurobiology, models and cognition. *Progress in Neurobiology* *158*, 132–152.  
949 10.1016/j.pneurobio.2017.07.002.
- 950 81. Deco, G., Jirsa, V., McIntosh, A.R., Sporns, O., and Kötter, R. (2009). Key role of coupling,  
951 delay, and noise in resting brain fluctuations. *Proceedings of the National Academy of  
952 Sciences of the United States of America* *106*, 10302–10307. 10.1073/pnas.0901831106.
- 953 82. Gollo, L.L., Roberts, J.A., and Cocchi, L. (2017). Mapping how local perturbations influence  
954 systems-level brain dynamics. *NeuroImage* *160*, 97–112. 10.1016/j.neuroimage.2017.01.057.
- 955 83. Pang, J.C., Gollo, L.L., and Roberts, J.A. (2021). Stochastic synchronization of dynamics on  
956 the human connectome. *NeuroImage* *229*, 117738. 10.1016/j.neuroimage.2021.117738.

957  
958  
**959 ACKNOWLEDGMENTS**

960 We thank John Murray, Alex Fornito, and Luke Hearne for valuable scientific discussions. Human  
961 HCP data used for replication of results were provided by the Human Connectome Project, Wu-  
962 Minn Consortium (Principal Investigators: David Van Essen and Kamil Ugurbil; 963  
1U54MH091657) funded by the 16 NIH Institutes and Centers that support the NIH Blueprint for  
964 Neuroscience Research, and by the McDonnell Center for Systems Neuroscience at Washington  
965 University. This work was supported by National Health and Medical Research Council grants  
966 11144936 and 1145168 to J.A.R, Netherlands Organization for Scientific Research grants  
967 ALWOP.179, VIDI (452-16-015), and European Research Council Consolidator grant 101001062  
968 to M.P.V.D.H., and National Health and Medical Research Council grants 1138711 and 2001283  
969 to L.C.

970  
971  
**972 AUTHOR CONTRIBUTIONS**

973 Conceptualization: J.C.P., J.A.R., M.P.V.D.H., L.C.; Methodology: J.C.P., J.A.R., M.P.V.D.H.,  
974 L.C.; Software: J.C.P.; Formal analysis: J.C.P.; Investigation: J.C.P., J.K.R., J.A.R., M.P.V.D.H.,  
975 L.C.; Resources: J.A.R., M.P.V.D.H.; Visualization: J.C.P., J.A.R., M.P.V.D.H., L.C.; Funding  
976 acquisition: J.A.R., M.P.V.D.H., L.C.; Supervision: J.A.R., L.C.; Writing – original draft: J.C.P.,  
977 L.C.; Writing – review & editing: J.C.P., J.K.R., J.A.R., M.P.V.D.H., L.C.

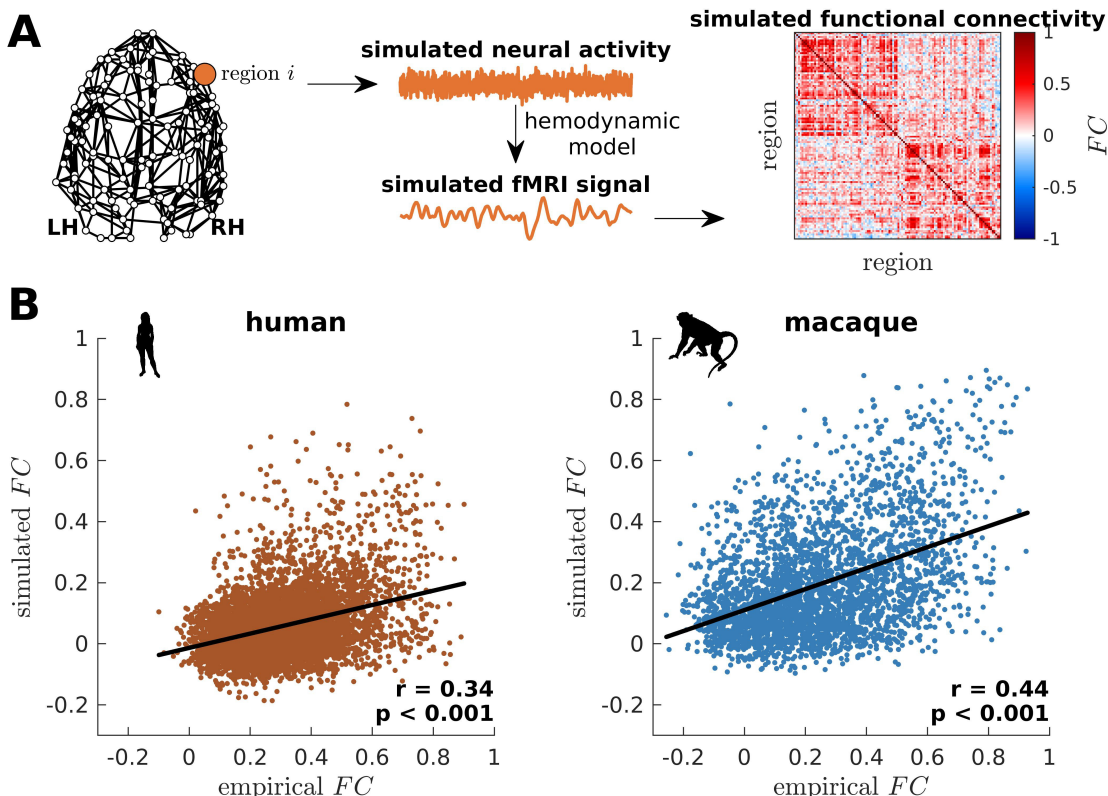
978  
979  
**980 COMPETING INTERESTS**

981 The authors declare no competing interests.

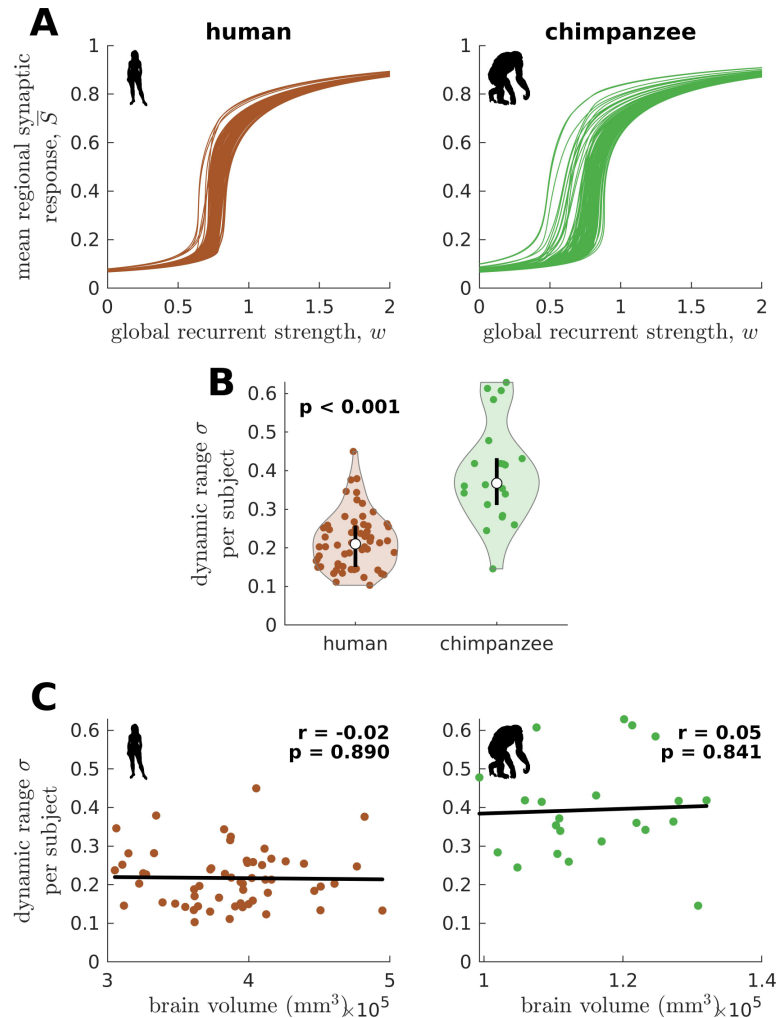
984 **SUPPLEMENTARY INFORMATION**

985

986

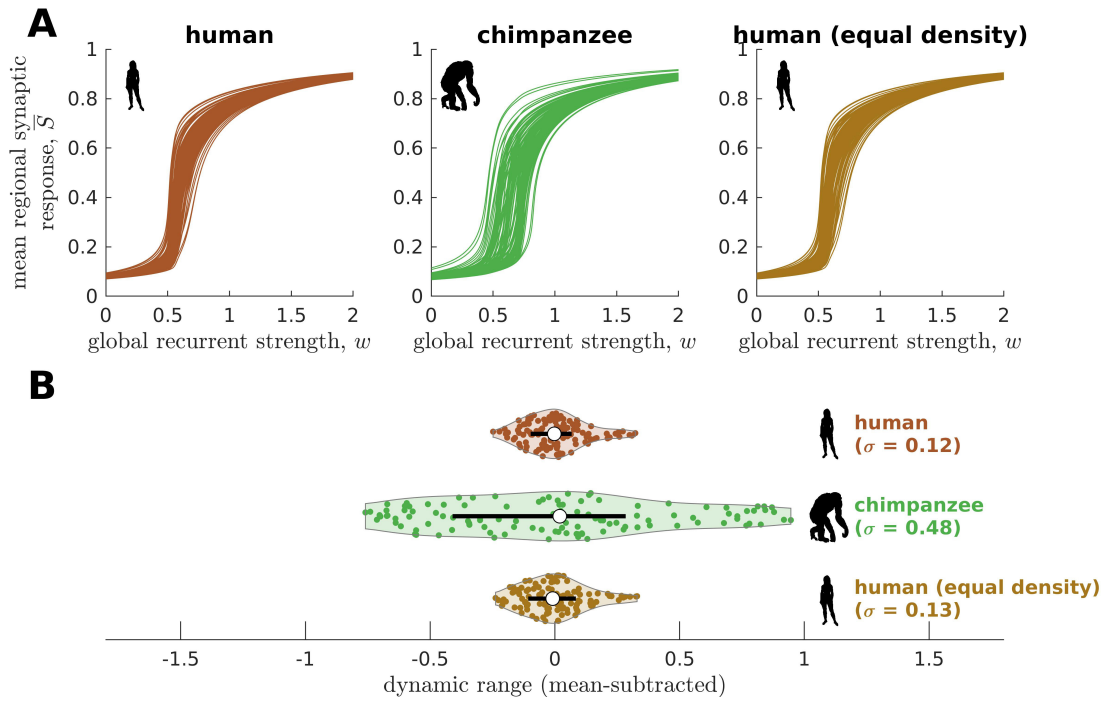
987  
988

989 **Fig. S1. Validation of simulated dynamics on empirical functional neuroimaging data.** (A) From the  
 990 connectome, neural activity is simulated using the model presented in Fig. 2B. This activity is fed into a  
 991 hemodynamic model to obtain a simulated fMRI signal for each brain region. Finally, functional  
 992 connectivity (FC) is calculated by taking pairwise Pearson correlations of the simulated fMRI signals across  
 993 all regions. (B) Association between simulated and empirical functional connectivity for humans and  
 994 macaques. The simulated functional connectivity is calculated using model parameters that optimize model-  
 995 data fitting. Each dot represents the pairwise FC. The solid line represents a linear fit with Pearson's  
 996 correlation coefficient ( $r$ ) and p-value ( $p$ ).



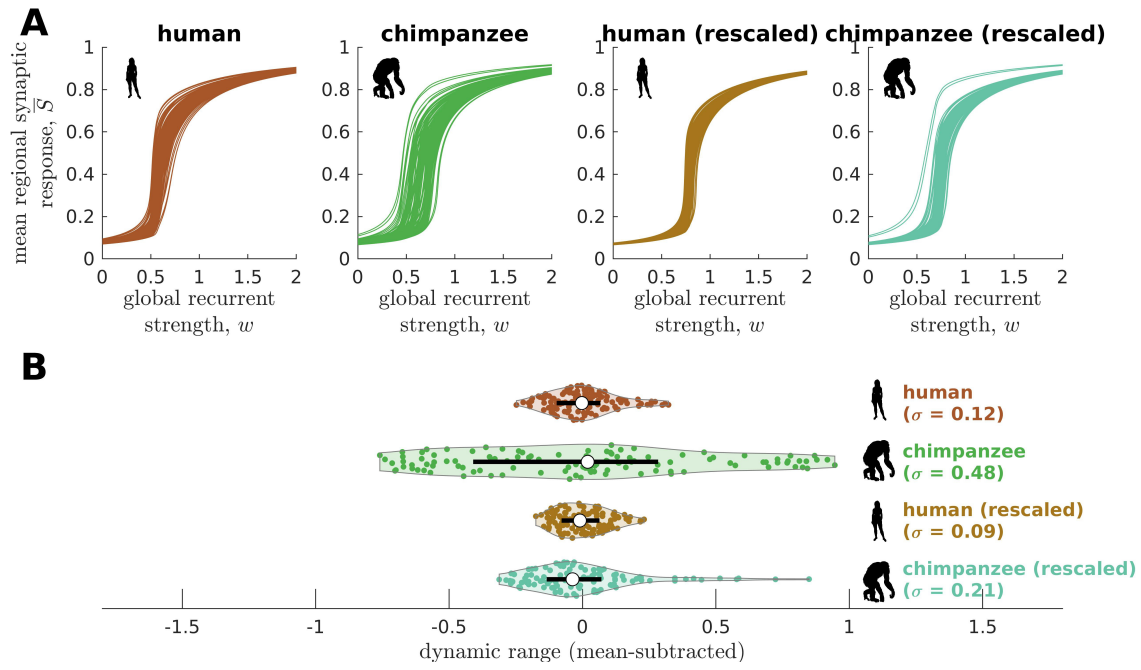
997  
998  
999  
1000  
1001  
1002  
1003  
1004  
1005  
1006

**Fig. S2. Confirmatory analysis on individual-specific connectomes and accounting for total brain volume.** (A) Regional neural dynamics as a function of global recurrent strength ( $w$ ) for exemplar human and chimpanzee participants. (B) Violin plot of the standard deviation ( $\sigma$ ) of the distribution of dynamic ranges across brain regions for each participant. Each violin shows the first to third quartile range (black line), median (white circle), raw data (dots), and kernel density estimate (outline).  $p$  is the p-value of the difference in the mean of the distribution between the species (two-sample t-test). (C) Dynamic range standard deviation ( $\sigma$ ) for each participant as a function of total brain volume. The solid line represents a linear fit with Pearson's correlation coefficient ( $r$ ) and p-value ( $p$ ).



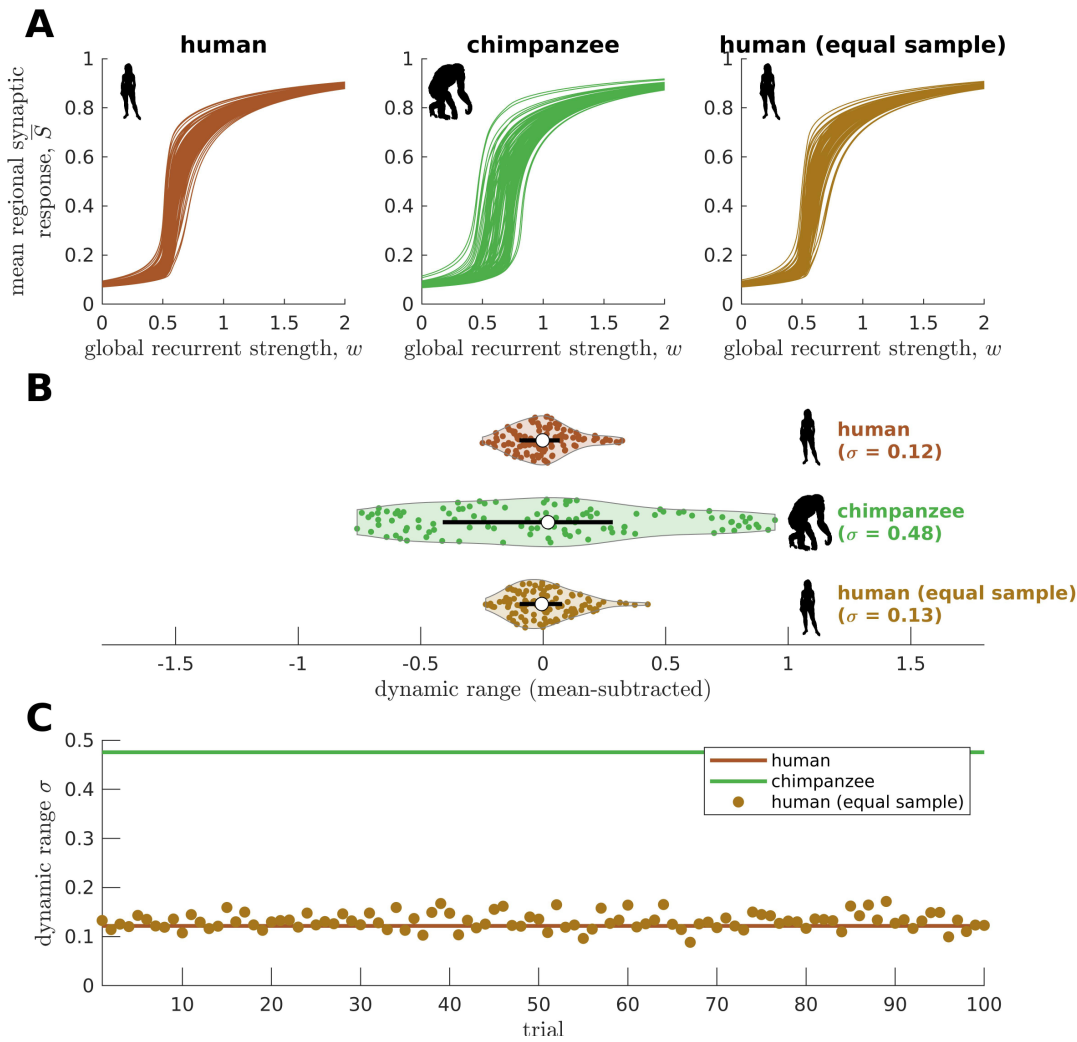
1007  
1008  
1009  
1010  
1011  
1012  
1013  
1014  
1015

**Fig. S3. Confirmatory analysis on human and chimpanzee connectomes of equal connection density.**  
 (A) Regional neural dynamics as a function of global recurrent strength ( $w$ ) for the original human connectome, original chimpanzee connectome, and human connectome pruned to have an equal density as the original chimpanzee connectome. (B) Violin plot of the distribution of dynamic ranges across brain regions. Each violin shows the first to third quartile range (black line), median (white circle), raw data (dots), and kernel density estimate (outline). The data are mean-subtracted for visual purposes.  $\sigma$  is the standard deviation of the distribution.

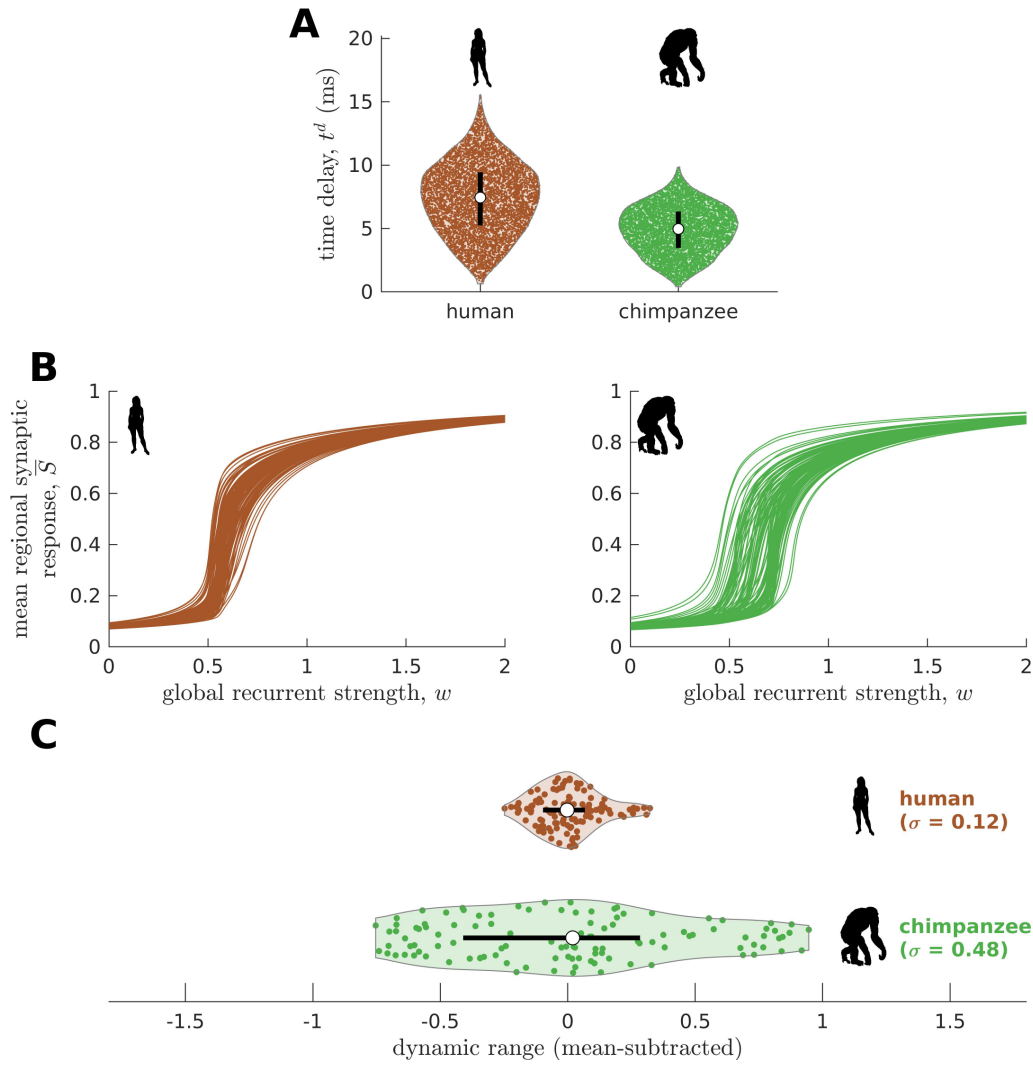


1016  
1017  
1018  
1019  
1020  
1021  
1022  
1023  
1024  
1025

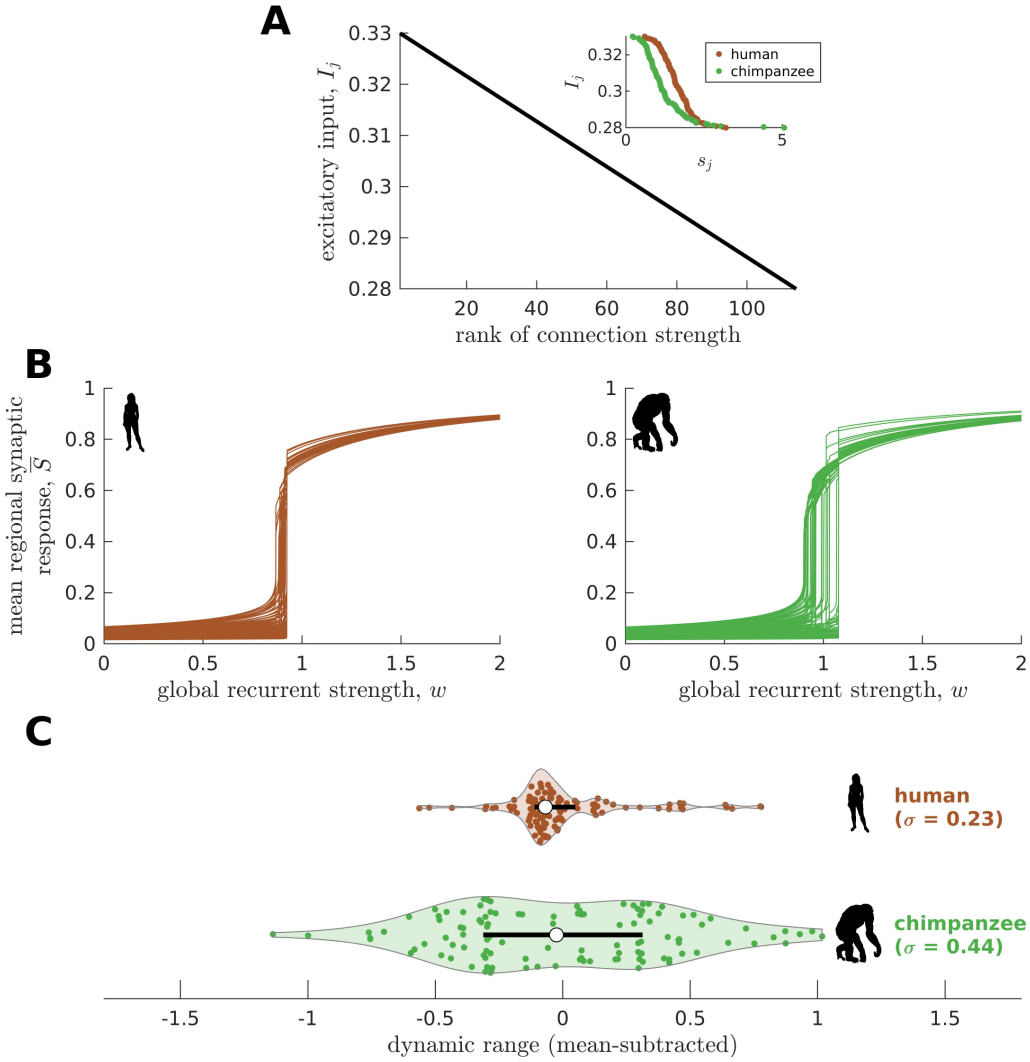
**Fig. S4. Confirmatory analysis accounting for inter-individual variability of connectomic data.** (A) Regional neural dynamics as a function of global recurrent strength ( $w$ ) for the original human connectome, original chimpanzee connectome, human connectome rescaled to match the inter-individual variability of the original chimpanzee connectome, and chimpanzee connectome rescaled to match the inter-individual variability of the original human connectome. (B) Violin plot of the distribution of dynamic ranges across brain regions. Each violin shows the first to third quartile range (black line), median (white circle), raw data (dots), and kernel density estimate (outline). The data are mean-subtracted for visual purposes.  $\sigma$  is the standard deviation of the distribution.



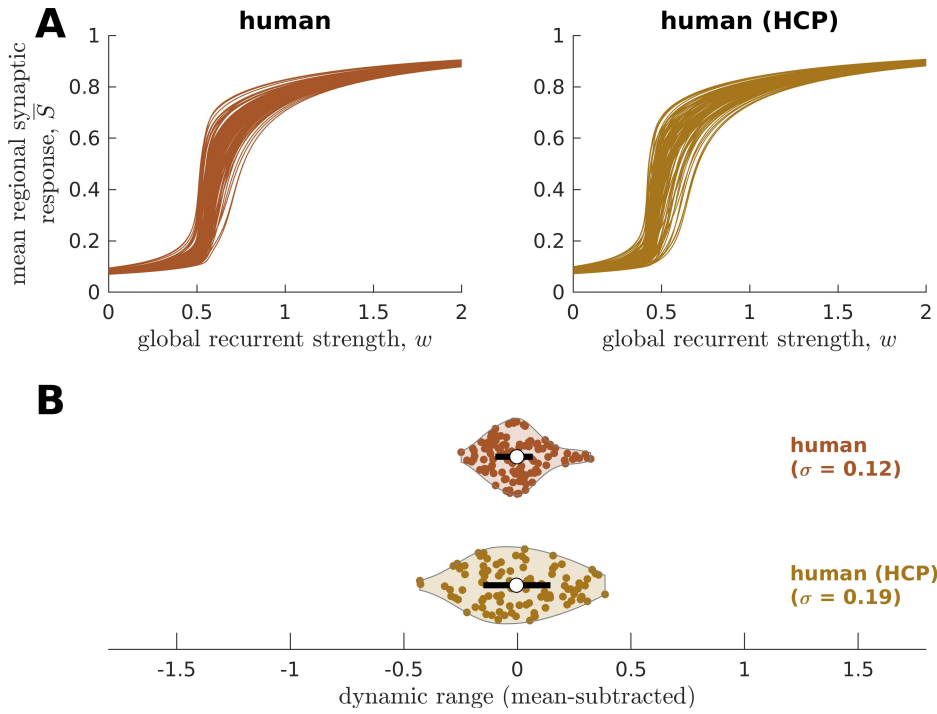
1028 **Fig. S5. Confirmatory analysis on matched sample size.** (A) Regional neural dynamics as a function of  
1029 global recurrent strength ( $w$ ) for the original human connectome, original chimpanzee connectome, and an  
1030 exemplar human connectome averaged from a sample of random human participants of the same size as  
1031 the chimpanzee group ( $N = 22$ ). (B) Violin plot of the distribution of dynamic ranges across brain regions.  
1032 Each violin shows the first to third quartile range (black line), median (white circle), raw data (dots), and  
1033 kernel density estimate (outline). The data are mean-subtracted for visual purposes.  $\sigma$  is the standard  
1034 deviation of the distribution. (C) Dynamic range standard deviation ( $\sigma$ ) for multiple random sampling trials  
1035 of human participants. The solid lines represent the results for the original human and chimpanzee  
1036 connectomes.



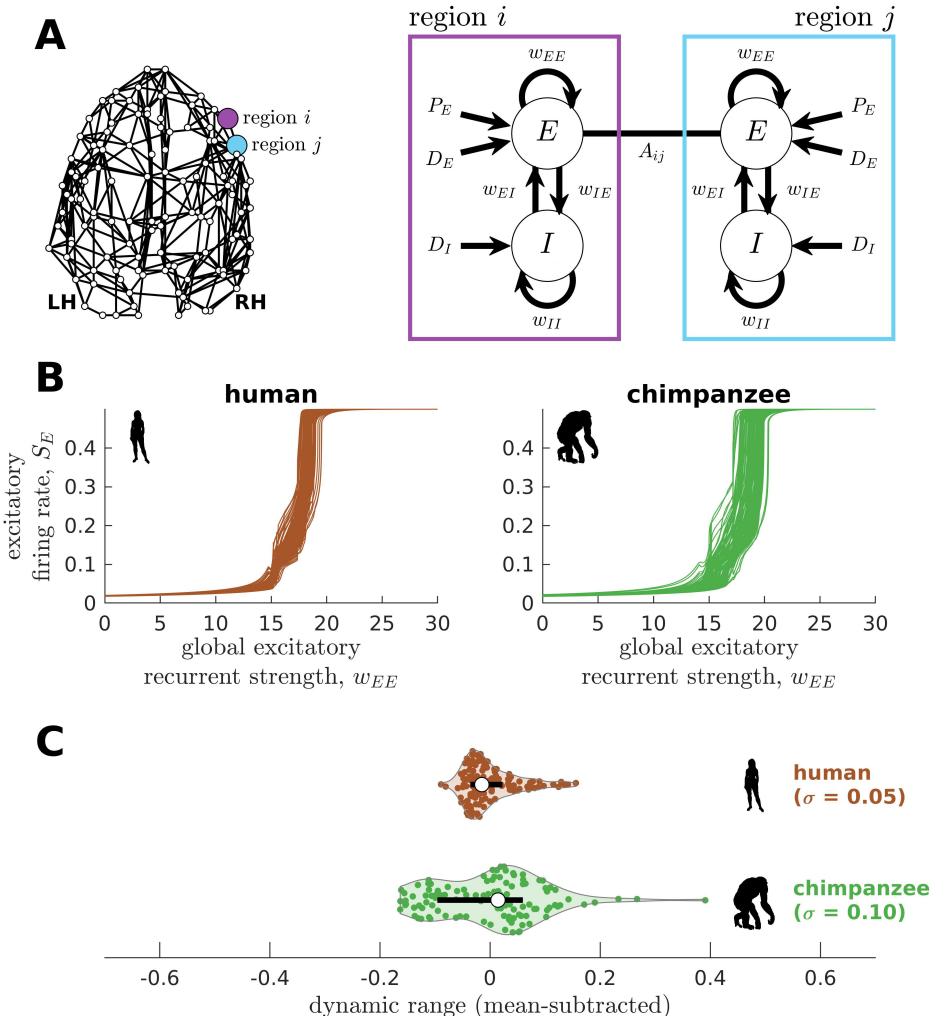
1039 **Fig. S6. Confirmatory analysis accounting for activity propagation delays between brain regions.** (A)  
1040 Violin plot of the distribution of propagation time delays ( $t^d$ ) across all connections for a representative  
1041 human and chimpanzee. Each violin shows the first to third quartile range (black line), median (white  
1042 circle), raw data (dots), and kernel density estimate (outline). (B) Regional neural dynamics as a function  
1043 of global recurrent strength ( $w$ ). (C) Violin plot of the distribution of dynamic ranges across brain regions.  
1044 Each violin shows the first to third quartile range (black line), median (white circle), raw data (dots), and  
1045 kernel density estimate (outline). The data are mean-subtracted for visual purposes.  $\sigma$  is the standard  
1046 deviation of the distribution.  
1047



1050 **Fig. S7. Confirmatory analysis accounting for heterogeneous excitatory input across brain regions.**  
 1051 (A) The excitatory input in each brain region  $I_j$  is inversely proportional to the rank of its total connection  
 1052 strength ( $s_j$ ). The inset shows the actual relationship between  $I_j$  and  $s_j$ . (B) Regional neural dynamics as a  
 1053 function of global recurrent strength ( $w$ ). (C) Violin plot of the distribution of dynamic ranges across brain  
 1054 regions. Each violin shows the first to third quartile range (black line), median (white circle), raw data  
 1055 (dots), and kernel density estimate (outline). The data are mean-subtracted for visual purposes.  $\sigma$  is the  
 1056 standard deviation of the distribution.

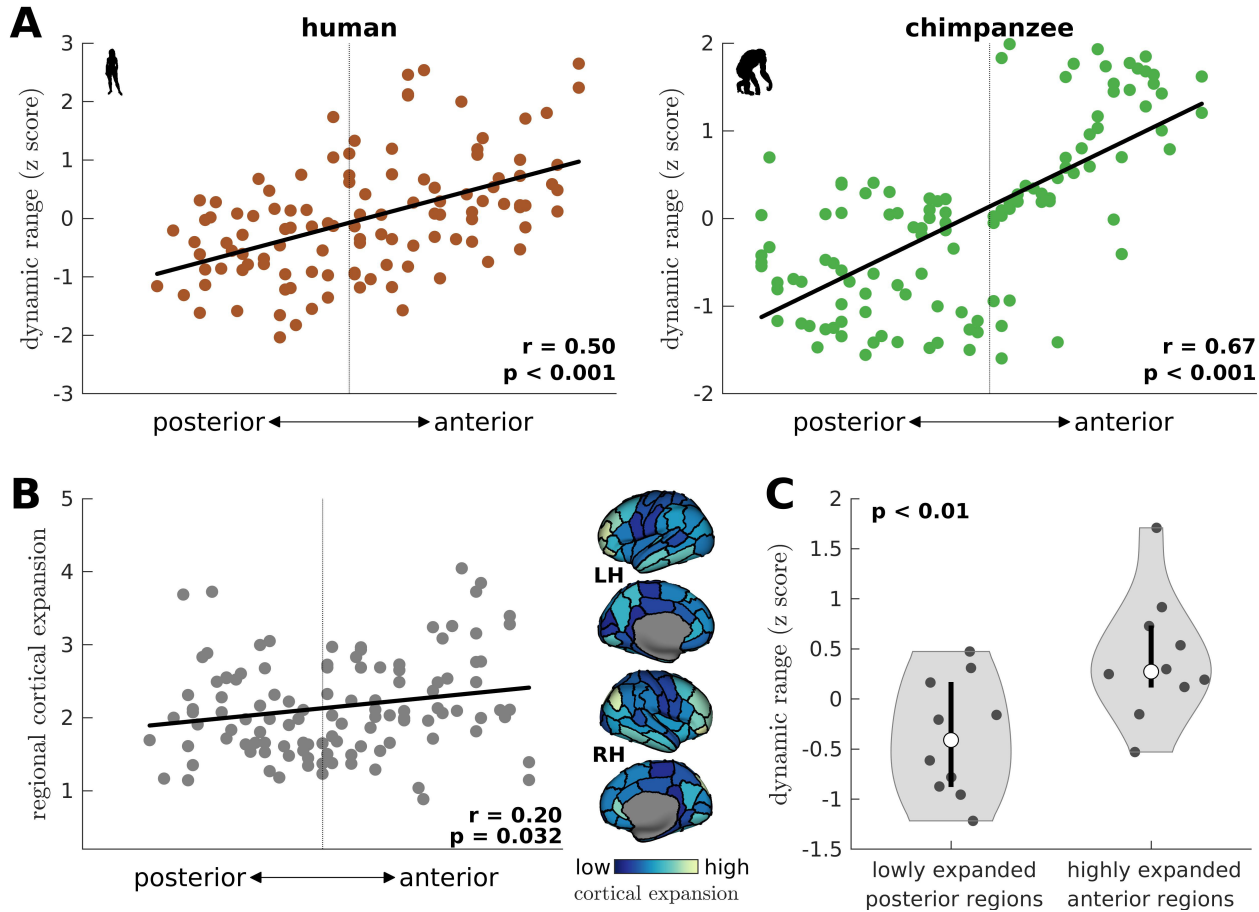


1059 **Fig. S8. Replication of human neural dynamics on an independent dataset.** (A) Regional neural  
1060 dynamics as a function of global recurrent strength ( $w$ ) for the original human connectome and human  
1061 connectome obtained from the Human Connectome Project (HCP). (B) Violin plot of the distribution of  
1062 dynamic ranges across brain regions. Each violin shows the first to third quartile range (black line), median  
1063 (white circle), raw data (dots), and kernel density estimate (outline). The data are mean-subtracted for visual  
1064 purposes.  $\sigma$  is the standard deviation of the distribution.



1065  
1066  
1067  
1068  
1069  
1070  
1071  
1072  
1073  
1074  
1075  
1076  
1077  
1078  
1079

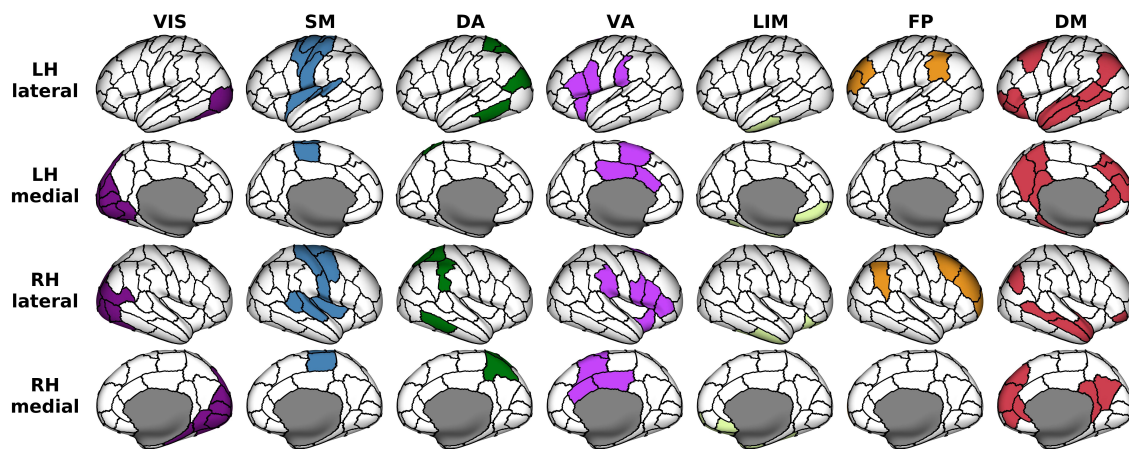
**Fig. S9. Replication of human and chimpanzee neural dynamics using a different biophysical model (the Wilson-Cowan model).** (A) Exemplar connectome and schematic diagram of the Wilson-Cowan model. In this biophysical model, each brain region comprises interacting populations of excitatory (*E*) and inhibitory (*I*) neurons. Connections within and between populations are represented by the *w* parameters; e.g.,  $w_{EE}$  represents the excitatory recurrent connection strength. The excitatory neural population is driven by a constant excitatory input  $P_E$  and white noise with standard deviation  $D_E$ , while the inhibitory population is only driven by white noise with standard deviation  $D_I$ . Regions *i* and *j* are connected with weight  $A_{ij}$  based on the connectomic data. (B) Regional neural dynamics (mean excitatory firing rate  $S_E$ ) as a function of global excitatory recurrent strength ( $w_{EE}$ ). (C) Violin plot of the distribution of dynamic ranges across brain regions. Each violin shows the first to third quartile range (black line), median (white circle), raw data (dots), and kernel density estimate (outline). The data are mean-subtracted for visual purposes.  $\sigma$  is the standard deviation of the distribution.



1080  
1081  
1082  
1083  
1084  
1085  
1086  
1087  
1088  
1089  
1090  
1091  
1092  
1093  
1094  
1095

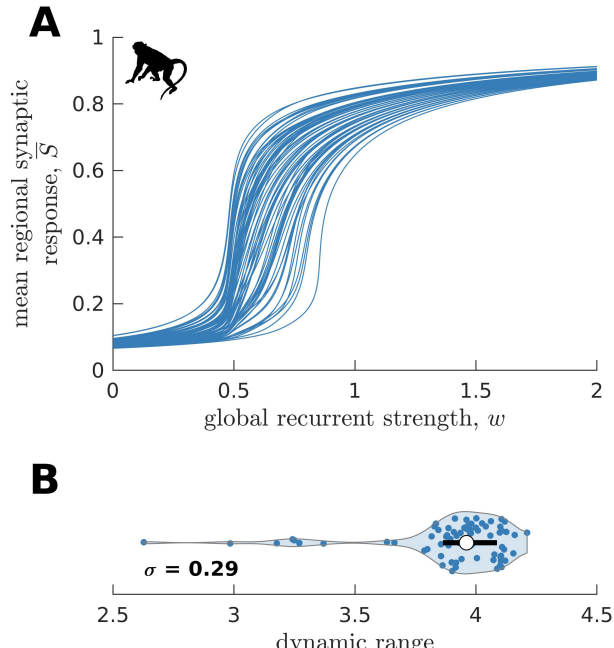
**Fig. S10. Gradient of dynamic ranges and regional chimpanzee-to-human cortical expansion along the anterior-posterior axis.** (A) Relationship between a brain region's dynamic range and its anterior-posterior location. The dynamic range values are transformed to z scores. The solid line represents a linear fit with Pearson's correlation coefficient ( $r$ ) and p-value ( $p$ ). (B) Relationship between a brain region's cortical expansion and its anterior-posterior location. The expansion is defined as the human:chimpanzee surface area ratio of each region, following [27]. The solid line represents a linear fit with Pearson's correlation coefficient ( $r$ ) and p-value ( $p$ ). The level of expansion is visualized on inflated human cortical surfaces. Light color represents a highly expanded region in humans compared to chimpanzees, while dark color represents a lowly expanded region. (C) Violin plot of the distribution of dynamic ranges of highly expanded anterior regions (top 10 regions) and lowly expanded posterior regions (bottom 10 regions) in the human brain. Each violin shows the first to third quartile range (black line), median (white circle), raw data (dots), and kernel density estimate (outline).  $p$  is the p-value of the difference in the mean of the distributions (two-sample t-test).

1096  
1097

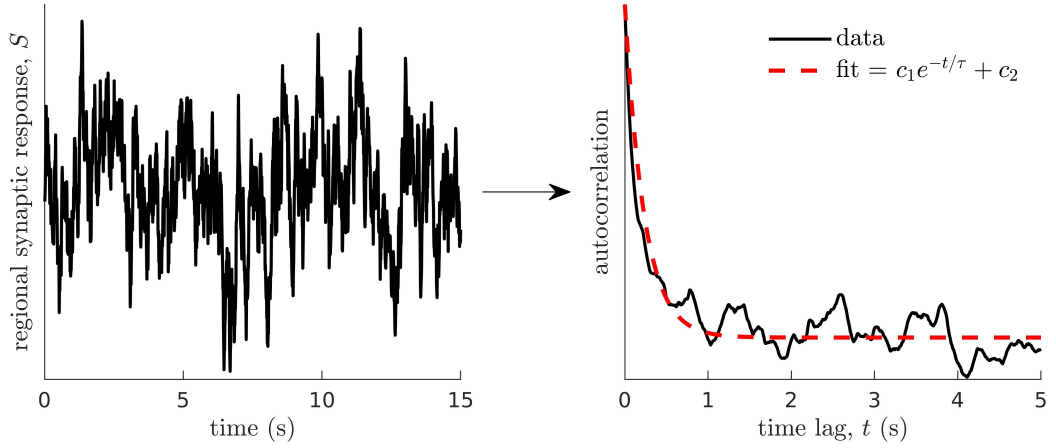


1098  
1099

1100 **Fig. S11. Anatomical locations of regions clustered according to seven canonical brain networks.** VIS  
1101 = Visual; SM = Somatomotor; DA = Dorsal Attention; VA = Ventral Attention; LIM = Limbic; FP =  
1102 Frontoparietal; DM = Default Mode. These functional networks are mapped onto the 114-region atlas in  
1103 Table S1. The networks are visualized on inflated human cortical surfaces.

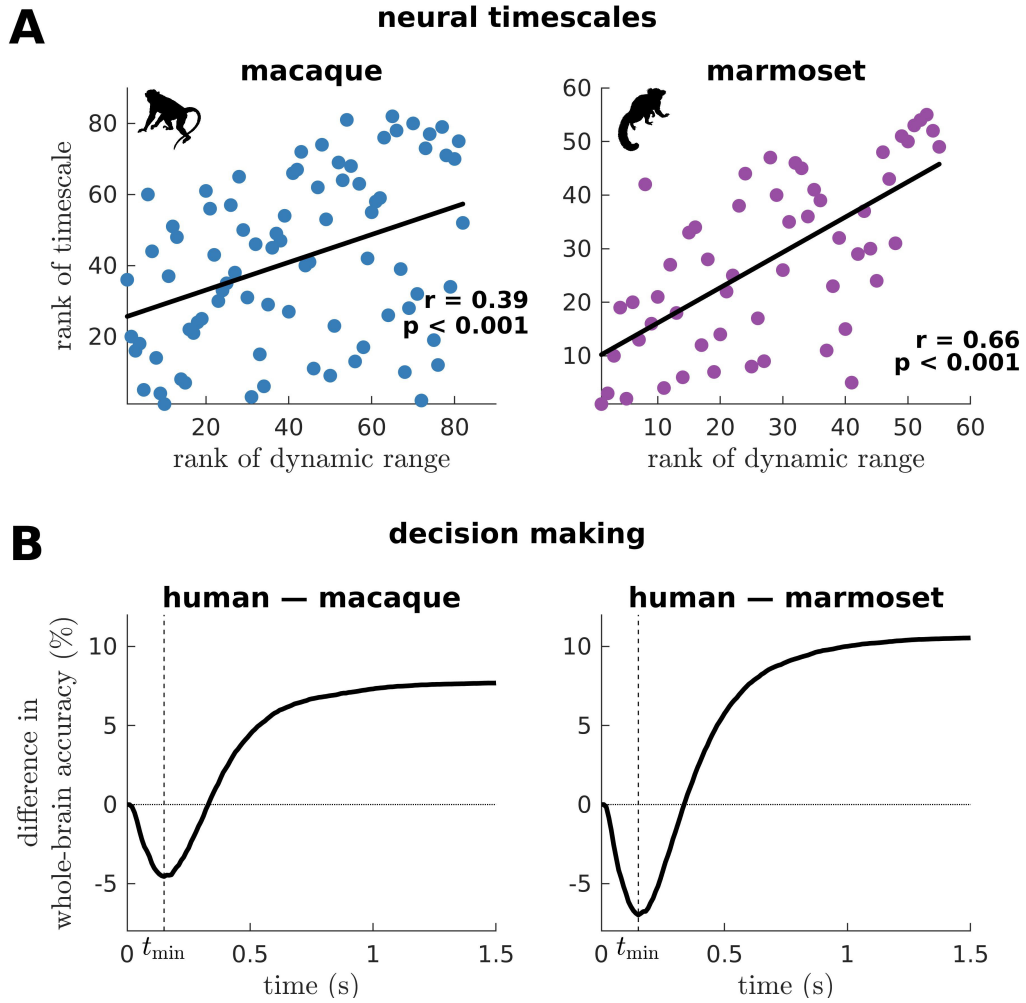


1104  
1105  
1106 **Fig. S12. Replication of macaque neural dynamics on an independent dataset (CoCoMac).** (A)  
1107 Regional neural dynamics as a function of global recurrent strength ( $w$ ). (B) Violin plot of the distribution  
1108 of dynamic ranges across brain regions. The violin shows the first to third quartile range (black line), median  
1109 (white circle), raw data (dots), and kernel density estimate (outline).  $\sigma$  is the standard deviation of the  
1110 distribution.



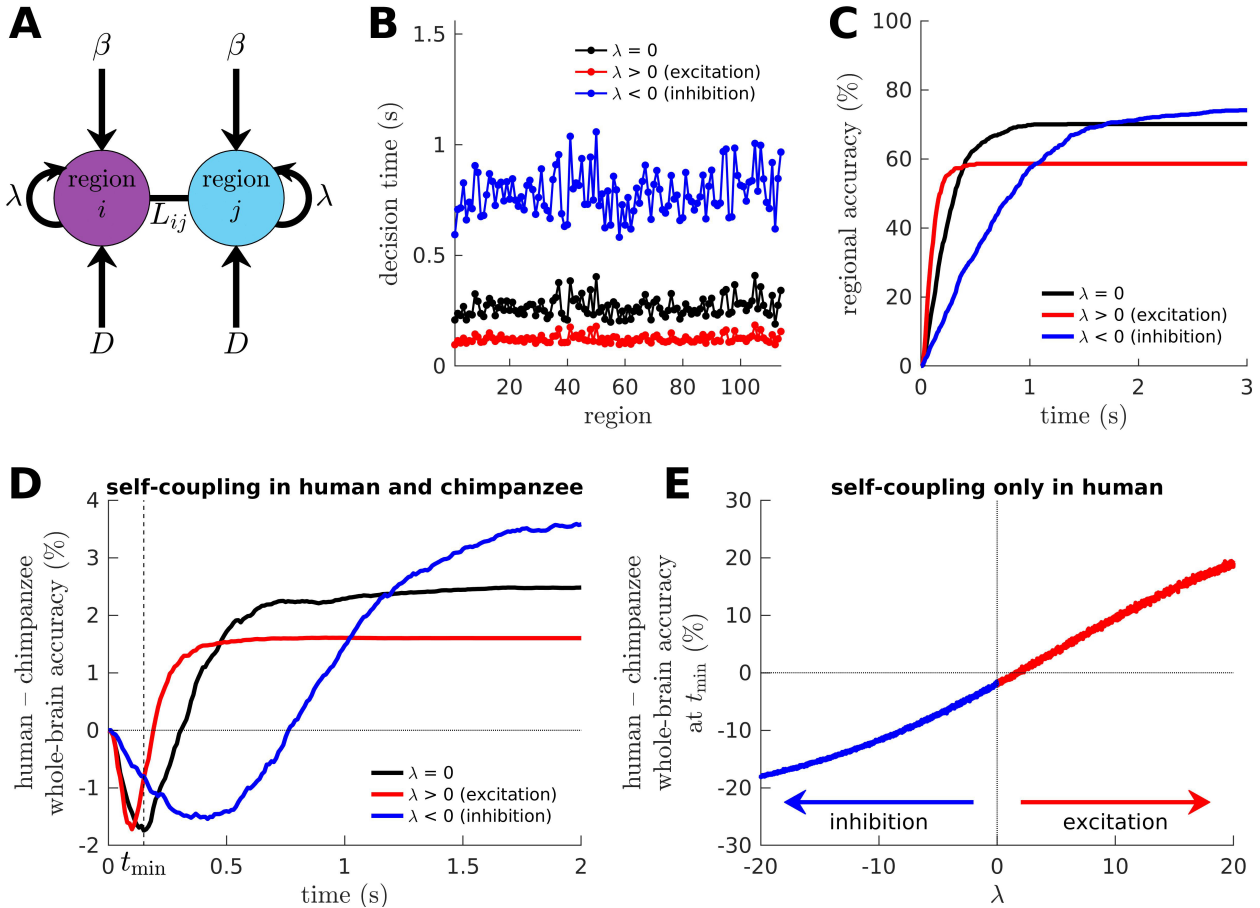
1111  
1112  
1113  
1114  
1115  
1116

**Fig. S13. Method for calculating neural timescales.** (Left) Sample regional neural activity. (Right) Autocorrelation of the data (neural activity) as a function of time lag (solid line) and corresponding exponential fit (dashed line) from which the timescale  $\tau$  is estimated. Note that  $c_1$  and  $c_2$  are fitting constants.



1117  
1118  
1119  
1120  
1121  
1122  
1123  
1124

**Fig. S14. Macaque and marmoset neural timescales and their connectome's decision-making capacity.** (A) Ranked neural timescales as a function of ranked dynamic ranges (similar to Fig. 6A). The solid line represents a linear fit with Pearson's correlation coefficient ( $r$ ) and p-value ( $p$ ). (B) Human-macaque and human-marmoset difference in whole-brain accuracy across time (similar to Fig. 6E). The dashed line shows the time ( $t_{\min}$ ) at which the difference in accuracy is most negative (i.e., macaque accuracy > human accuracy and marmoset accuracy > human accuracy).



1127 **Fig. S15. Effects of excitation and inhibition on decision-making capacity of the human and**  
1128 **chimpanzee connectomes.** (A) Extended drift-diffusion model, which includes a  $\lambda$  parameter that scales

1129 the self-coupling term.  $\lambda = 0$  corresponds to our original drift-diffusion model,  $\lambda > 0$  corresponds to

1130 increased excitation, and  $\lambda < 0$  corresponds to increased inhibition. (B) Decision time of each brain region,

1131 which is quantified as the time it takes for the region to reach its decision threshold. (C) Decision accuracy

1132 across time of a region. (D) Difference in whole-brain accuracy across time between humans and

1133 chimpanzees. Note that both humans and chimpanzees have the same level of excitation or inhibition (i.e.,

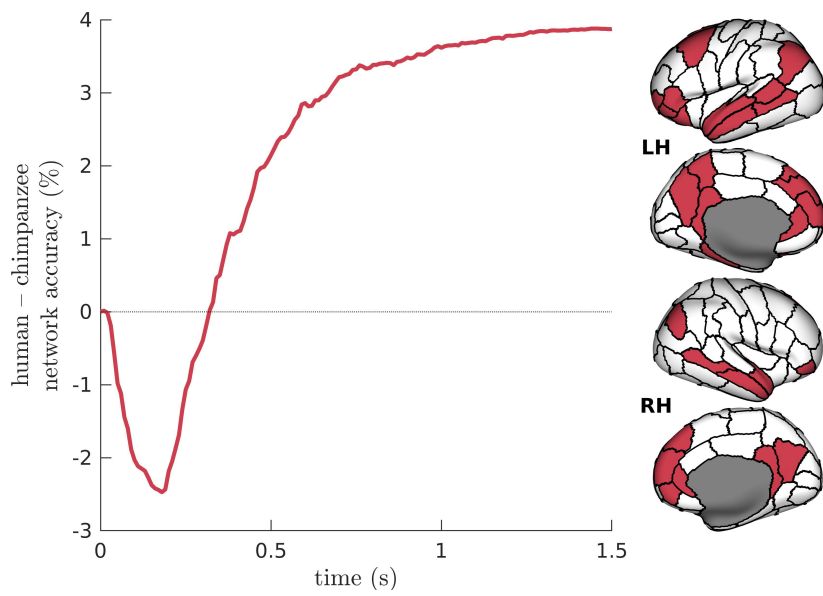
1134 their  $\lambda$  parameters are the same). The dashed line shows the time ( $t_{\min}$ ) at which the difference in accuracy

1135 between humans and chimpanzees is most negative at  $\lambda = 0$  (i.e., chimpanzee accuracy  $>$  human accuracy).

1136 (E) Difference in whole-brain accuracy at  $t_{\min}$  (found in panel D) between humans and chimpanzees, with

1137 only the humans having a non-zero self-coupling term. Hence,  $\lambda \neq 0$  for humans and  $\lambda = 0$  for

1138 chimpanzees.



1139

1140

1141 **Fig. S16. Difference in Default-Mode Network (DMN) accuracy across time between humans and**  
1142 **chimpanzees.** The DMN regions are visualized on inflated human cortical surfaces.

1143

**Table S1. List of 57 cortical regions in each hemisphere.**

bankssts_1	middle temporal_1	rostral middle frontal_1
caudal anterior cingulate_1	middle temporal_2	rostral middle frontal_2
caudal middle frontal_1	parahippocampal_1	rostral middle frontal_3
cuneus_1	paracentral_1	superior frontal_1
entorhinal_1	parsopercularis_1	superior frontal_2
fusiform_1	parsorbitalis_1	superior frontal_3
fusiform_2	parstriangularis_1	superior frontal_4
inferior parietal_1	pericalcarine_1	superior parietal_1
inferior parietal_2	postcentral_1	superior parietal_2
inferior temporal_1	postcentral_2	superior parietal_3
inferior temporal_2	postcentral_3	superior temporal_1
isthmus cingulate_1	posterior cingulate_1	superior temporal_2
lateral occipital_1	precentral_1	supramarginal_1
lateral occipital_2	precentral_2	supramarginal_2
lateral orbitofrontal_1	precentral_3	frontal pole_1
lateral orbitofrontal_2	precentral_4	temporal pole_1
lingual_1	precuneus_1	transverse temporal_1
lingual_2	precuneus_2	insula_1
medial orbitofrontal_1	rostral anterior cingulate_1	insula_2

1144

1145